Merger of binary white dwarf–neutron stars: Simulations in full general relativity

Vasileios Paschalidis,[1] Yuk Tung Liu,[1] Zachariah Etienne,[1] and Stuart L. Shapiro[1,2]

[1]*Department of Physics, University of Illinois at Urbana-Champaign, Urbana, Illinois 61801, USA*

[2]*Department of Astronomy and NCSA, University of Illinois at Urbana-Champaign, Urbana, Illinois 61801, USA*

(Received 26 July 2011; published 18 November 2011)

We perform fully general relativistic simulations to address the inspiral and merger of binary white dwarf–neutron stars. The initial binary is in a circular orbit at the Roche critical separation. The goal is to determine the ultimate fate of such systems. We focus on binaries whose total mass exceeds the maximum mass ($M_{\rm max}$) a cold, degenerate equation of state can support against gravitational collapse. The time and length scales span many orders of magnitude, making fully general relativistic hydrodynamic simulations computationally prohibitive. For this reason, we model the white dwarf as a ''pseudo—white dwarf'' as in our binary white dwarf–neutron star (WDNS) head-on collisions study [V. Paschalidis, Z. Etienne, Y. T. Liu, and S. L. Shapiro, Phys. Rev. D **83**, 064002 (2011)]. Our general relativistic hydrodynamic simulations of a pseudo-WDNS (pWDNS) system with a $0.98M_\odot$ white dwarf and a $1.4M_\odot$ neutron star show that the merger remnant is a spinning Thorne-Zytkow-like object (TZlO) surrounded by a massive disk. The final total rest mass exceeds $M_{\rm max}$, but the remnant does not collapse promptly. To assess whether the object will ultimately collapse after cooling, we introduce radiative thermal cooling. We first apply our cooling algorithm to TZlOs formed in pWDNS head-on collisions, and show that these objects collapse and form black holes on the cooling time scale, as expected. However, when we cool the spinning TZlO formed in the merger of a circular-orbit pWDNS binary, the remnant does not collapse, demonstrating that differential rotational support is sufficient to prevent collapse. Given that the final total mass exceeds $M_{\rm max}$ for our cold equation of state, magnetic fields and/or viscosity may redistribute angular momentum, ultimately leading to delayed collapse to a black hole. We infer that the merger of realistic massive WDNS binaries likely will lead to the formation of spinning TZlOs that undergo delayed collapse.

DOI: 10.1103/PhysRevD.84.104032 PACS numbers: 04.25.D−, 04.25.dk, 04.40.Dg

I. INTRODUCTION

During inspiral and merger, compact binaries emit a large flux of gravitational waves (GWs), making them among the most promising sources for GWs detectable by ground-based laser interferometers like LIGO [1,2], VIRGO [3,4], GEO [5], TAMA [6,7] and AIGO [8], as well as by proposed space-based interferometers such as LISA [9] and DECIGO [10]. Extracting physical information about these binaries from their GWs may shed light on determining their ultimate fate, but requires careful modeling of these systems in full general relativity (see [11] for review and references therein). Most effort to date has focused on modeling black hole–black hole (BHBH) binaries (see [12] and references therein), and neutron star–neutron star (NSNS) binaries (see [13] for a review), with some recent work on black hole–neutron star (BHNS) binaries in full general relativity (GR)[14–32].

As a follow-up to our investigation of binary white dwarf–neutron star (WDNS) *head-on* collisions [33], in this work we perform fully general relativistic simulations of *circular-orbit* WDNS binaries through inspiral and merger. Throughout we call this the ''inspiral case'' to distinguish it from the ''head-on'' collision case. WDNS binaries are promising sources of low-frequency GWs (for LISA and DECIGO) and, as we argued in [34], possibly also high-frequency GWs (for LIGO, VIRGO, GEO, TAMA and AIGO), if the remnant ultimately collapses to a black hole.

Like neutron star–neutron star binaries, WDNS binaries are known to exist. In [34] we compiled tables of 20 observed WDNS binaries and their measured orbital properties. The NS masses in these systems range between $1.26M_\odot$ and $2.08M_\odot$, and their distribution is centered around $1.5M_\odot$. On the other hand, the WD masses in these systems range between $0.125M_\odot$ and $1.3M_\odot$, and their distribution is centered around $0.6M_\odot$. Eighteen of these observed WDNS binaries have total mass greater than $1.65M_\odot$, 8 of which have a WD component with mass greater than $0.8M_\odot$, and 5 have total mass greater than $2.2M_\odot$. This is interesting because the expected Tolman-Oppenheimer-Volkoff (TOV) limiting mass for a cold, degenerate gas must be larger than $1.97M_\odot$ [35] and may reach $2.2M_\odot$ [36–44], depending on the equation of state (EOS). One of the main goals of this work is to determine whether a WDNS merger remnant will undergo prompt collapse to a black hole.

Population synthesis calculations [45,46] show that there are about 2.2×10^6 WDNS binaries in our Galaxy, and that they have a merger rate between 10^{-6} yr^{-1} and 1.4×10^{-4} yr^{-1}. Furthermore, these studies find that after a year of integration, LISA-like interferometers should be

able to detect 1–40 WDNS premerger binaries. Recent work by Thompson, Kistler, and Stanek [47] suggests that the lower limit on the merger rate of binary WDNSs in the Milky Way, at 95% confidence, is 2.5×10^{-5} yr^{-1}. Thompson, Kistler, and Stanek also suggest that the merger rate in the local universe is ~ 0.5–1×10^4 Gpc^{-3} yr^{-1}. Therefore, ignoring some uncertainties, all recent population synthesis calculations suggest that LISA-like projects should be able to detect a few WDNS premergers per year.

A. Previous WDNS work

In [34] we focused on possible evolutionary scenarios for circular WDNS binaries that have inspiraled sufficiently close that they reach the termination point for equilibrium configurations. This is the Roche limit for WDNSs, at which point the WD fills its Roche lobe and may experience one of at least two possible fates: (i) stable mass transfer (SMT) from the WD across the inner Lagrange point onto the NS, or (ii) tidal disruption of the WD by the NS via unstable mass transfer (UMT).

Note that once an UMT binary reaches the critical Roche separation, further inspiral and merger is governed by tidal effects and hydrodynamical interactions and not GW emission.

We also studied key parameters that determine whether a system will undergo SMT or UMT and found that, for a given NS mass, there exists a critical mass ratio $q_{\rm crit} \approx 0.5$ that separates the UMT and SMT regimes. If the mass ratio $q = M_{\rm WD}/M_{\rm NS}$ of a WDNS system is such that $q > q_{\rm crit}$, the WD quickly overfills its Roche lobe, and the binary will ultimately undergo UMT. In the opposite case, $q < q_{\rm crit}$, the system will undergo SMT. We showed that a quasistationary treatment is adequate to follow the evolution of an SMT binary during this secular phase and calculated the gravitational waveforms. We also pointed out that WDNS observations suggest that there are known candidates residing in both regimes.

In the case of tidal disruption (UMT), by contrast, the system will evolve on a hydrodynamical (orbital) time scale. In this scenario the NS may plunge into the WD and spiral into the center of the star, forming a quasiequilibrium configuration that resembles a Thorne-Zytkow object [48]; alternatively, the NS may be the receptacle of massive debris from the disrupted WD.

The ultimate fate of the merged WDNS depends on (1) the initial mass of the cold progenitor stars, (2) the degree of mass and angular momentum loss during the WD disruption and binary merger phases, (3) the angular momentum profile of the WDNS remnant, and (4) the extent to which disrupted debris is heated by shocks and/or nuclear reactions as it settles onto the NS and forms an extended, massive mantle. These are issues that require a hydrodynamic simulation to resolve. Note that Newtonian work on binaries with a WD component has been performed analytically in [34,49–53] and via Newtonian hydrodynamic simulations in [54–59]. However, ascertaining whether or not the neutron star ultimately undergoes catastrophic collapse (either prompt or delayed) to a black hole requires that such a simulation be performed in full general relativity. In fact, even the final fate of the NS in the alternative scenario in which there is a long epoch of SMT may also lead to catastrophic collapse, if the neutron star mass is close to the neutron star maximum mass. This scenario too will require a general relativistic hydrodynamic simulation to track.

In [33] we employed the Illinois adaptive mesh refinement (AMR) relativistic hydrodynamics code [23,60] to perform the first simulations of these systems in full GR. In particular, we studied the head-on collision from rest at large separation of a massive WD and a NS. We focused on compact objects whose total mass exceeds the maximum mass supportable by a cold EOS in order to determine the outcome of such collisions.

The vast range of time and length scales involved in the WDNS problem make fully general relativistic simulations extremely challenging. In [33] we demonstrated that the length scales span 4 orders of magnitude, as measured in neutron star radii, and that the associated time scales span 6 orders of magnitude in M, the total system mass. Current numerical relativity techniques and available computational resources make such simulations prohibitive. For this reason, we tackled this problem using a different strategy.

In particular, we constructed a six-parameter piecewise polytropic EOS which mimics realistic NS EOSs while, at the same time, scales down the size of the WD. We call these scaled-down WDs ''pseudo-WDs (pWDs).'' We chose all of the piecewise EOSs in such a way that the maximum NS mass is $1.8M_\odot$ [61], and the maximum WD mass is $1.43M_\odot$, i.e., the Chandrasekhar mass. Furthermore, we made sure these EOSs preserve the qualitative shape of the central density-mass curves as well as the number of stable and unstable NS and WD branches (see Figs. 1 and 2 in [33]). Moreover, the scaling is performed so that all the length-scale and time-scale inequalities of the realistic problem are left unchanged. For a given set of EOS parameters, a realistic WD has a counterpart pWD which has the same mass but is smaller in size. As a result, for every realistic WDNS system, we can construct a pseudo-WDNS (pWDNS) counterpart which involves the same (realistic) NS and the pWD counterpart of the WD.

Using pWDs we performed a sequence of head-on simulations in which the EOS is changed so that the pWDs have the same mass ($0.98M_\odot$) but decreasing compactions, while the compaction and mass of the NS involved remains practically unchanged. More precisely, while keeping the masses of the binary components and the NS radius fixed, the pWD compaction was modified so that the pWD:NS radius ratio varied between 5:1 and 20:1.

We then scaled the results of our simulations to predict the outcome in the realistic case: 500:1.

In addition to studying the effects of the pWD compaction, we also studied the effects of NS mass. We considered NSs with masses $1.4M_\odot$, $1.5M_\odot$, and $1.6M_\odot$.

All head-on collision simulations that we performed showed that after the collision 14%–18% of the initial total rest mass escapes to infinity. In all cases, the remnant rest mass exceeded the maximum rest mass that our *cold* EOS can support ($1.92M_\odot$), and no case led to prompt collapse to a black hole. This outcome arises because the final configurations become *hot*, due to shock heating. All our cases settle into a spherical quasiequilibrium configuration consisting of a cold NS core surrounded by a hot mantle. Hence, all remnants are Thorne-Zytkow-like objects (TZlOs). Scaling our results to realistic WD compactions, we predict that a realistic head-on collision will form a quasiequilibrium TZlO.

Although the head-on collision simulations appear to lead to a consistent result (the formation of a TZlO), these results cannot be used to predict the final fate of WDNS systems in circular orbit. On the one hand, one might expect that the remnant in the inspiraling case will collapse to a black hole, because shock heating is not likely to be as intense as in the head-on case. On the other hand, the large amount of angular momentum in the inspiraling binary case may work to prevent prompt collapse. Therefore, to predict whether the merged WDNS remnant will collapse, promptly or following cooling, we need to perform fully general relativistic simulations of WDNS binaries through inspiral and merger. Such mergers may also give rise to gamma ray bursts [62,63].

B. Goals and objectives

The purpose of the current work is threefold:

(a) We simulate the late inspiral and merger of a WDNS system consisting of a $1.4M_\odot$ NS and a $0.98M_\odot$ WD initially in circular orbit and at the Roche limit. As in our head-on collision studies, we employ the pWD approximation to make the computations feasible [64]. The pWD approximation is useful for predicting the ultimate fate of a realistic WDNS merger using scaling. In particular, the collision velocity (v_c) and the preshocked WD sound speed c_s both scale as $\sim(M/R_{\rm WD})^{1/2}$. This implies that the Mach number ($\mathcal{M} = v_c/c_s$) is invariant under scaling of $R_{\rm WD}$ and so is the degree of shock heating. The thermal energy, as well as the rotational kinetic energy (T) and the gravitational potential energy (W), all scale as $\sim M^2/R_{\rm WD}$, when the binary merges. Thus, $T/|W|$ is also invariant under scaling of $R_{\rm WD}$. These considerations simply mean that with respect to gravity the relative importance of thermal and rotational support in a WDNS merger remnant is approximately invariant, when the masses of the binary components are fixed and the only quantity that changes is the WD radius. As a consequence, the results obtained when adopting pWDNS systems can be scaled up to realistic WDNS systems. Note that our compaction study in [33] confirms the above scaling with the Mach number.

(b) We introduce a radiative cooling prescription and modify our adiabatic simulations by allowing for cooling to determine whether the merger remnant will collapse without thermal support, if it fails to collapse promptly. Otherwise, angular momentum provides sufficient support to prevent collapse.

(c) We allow cooling to occur in the TZlOs formed in our WDNS head-on collision simulations [33] to confirm that these remnants collapse to a black hole when the excess thermal energy is radiated away. In other words, we demonstrate that it is thermal pressure alone that prevents these objects from undergoing prompt collapse, since angular momentum support is completely absent in head-on collisions. Delayed collapse occurs on a cooling time scale in all cases, providing a consistency check on our cooling implementation.

Our pWDNS merger calculations show that the inspiral remnant is a spinning TZlO which is surrounded by a massive, extended, hot disk. In contrast to our head-on collisions, we do not find any outflows in the inspiraling case. Therefore, the final total mass is greater than the maximum mass supportable by our cold EOS and many nuclear EOSs. However, the remnant does not collapse promptly to a BH. We find that the remnant is both thermally and centrifugally supported. To determine whether centrifugal forces alone can support the remnant we incorporate cooling and find that the object does not collapse to a black hole. Therefore, the extra support provided by rotation is sufficient for preventing the collapse.

Even though the TZlO does not collapse after cooling, we expect delayed collapse ultimately because the final total rest mass ($\sim 2.5M_\odot$) is larger than the maximum possible mass supportable by our cold EOS (and many nuclear EOSs), even allowing for *uniform* rotation. (The maximum gravitational mass of a uniformly rotating star with our adopted EOS is $\simeq 2.1M_\odot$.) We expect that collapse to a BH will take place after viscosity or magnetic fields redistribute the angular momentum, as in the case of a hypermassive neutron star [65–67]. This conclusion will be true in the case of realistic WDNS mergers, unless the true nuclear EOS supports a uniformly rotating star with a rest mass exceeding the remnant mass. Many viable EOSs do not support rest masses as large as $2.5M_\odot$ [37], the remnant rest mass in our simulations.

This paper is organized as follows. In Sec. II the pWD approximation and the EOS adopted in our simulations are briefly reviewed. Section III outlines the initial data generation technique. Section IV summarizes the methods

used for evolving the gravitational and matter fields. Section V introduces our radiative cooling formalism, which is then applied to the TZlO remnants from our pWDNS head-on collision simulations in Sec. VI. We present the results of our fully relativistic hydrodynamic simulations of the binary pWDNS late inspiral and merger in Sec. VII, and turn on cooling in Sec. VII C. In Sec. VIII we discuss possible effects of nuclear reactions in realistic WDNS mergers and give estimates of realistic cooling and angular momentum redistribution time scales. Section IX concludes with a summary of the main findings. Throughout this work, geometrized units are adopted, where $G = c = 1$, unless otherwise specified.

II. EQUATION OF STATE

We employ the following 6-parameter piecewise polytropic cold EOS:

$$\frac{P}{\rho_0} = \begin{cases} \kappa_1 \rho_0^{1/n_1}, & \rho_0 \leq \rho_1 \\ \kappa_2 \rho_0^{1/n_2}, & \rho_1 < \rho_0 \leq \rho_2 \\ \kappa_3 \rho_0^{1/n_3}, & \rho_0 > \rho_2, \end{cases} \tag{1}$$

where P is the pressure, ρ_0 is the rest-mass density, and κ_1, κ_2, κ_3, n_1, n_2, n_3, ρ_1, ρ_2 are the parameters of the EOS. The parameters in Eq. (1) are 8 in number, but continuity requires that the following conditions be true:

$$\kappa_1 = \kappa_2 \rho_1^{1/n_2 - 1/n_1}, \qquad \kappa_2 = \kappa_3 \rho_2^{1/n_3 - 1/n_2}. \tag{2}$$

As a result, the adopted EOS has 6 free parameters: κ_3, n_1, n_2, n_3, ρ_1, and ρ_2.

Because of its multiple parameters, this EOS gives us the freedom to capture the same characteristic curves and turning points on a TOV mass-central density plot as for a realistic cold, degenerate EOS (see [68]), as shown in Fig. 1 in [33]. The EOS exhibits both stable ($dM/d\rho_{0,c} > 0$) and unstable ($dM/d\rho_{0,c} < 0$) branches for both WDs and NSs, as in the realistic case.

Furthermore, this EOS allows us to adjust the size of a pWD of any given mass, thereby shifting the pWD branch to smaller radii (see Fig. 2 in [33]), while keeping the NS branch approximately unchanged. For more details about our EOS and pWDs we refer the interested reader to [33].

In this work the EOS parameters correspond to the 10:1 EOS we considered in [33]: $\kappa_3 = 4993$, $\Gamma_1 = 1.515$, $\Gamma_2 = 2.969$, $\Gamma_3 = 0.714$, $\log(\rho_1/\rho_{\rm nuc}) = -2.268$, $\log(\rho_2/\rho_{\rm nuc}) = 0.208$, where all values are in geometrized units and $\Gamma_i = 1 + 1/n_i$, $\rho_{\rm nuc} = 1.485 \times 10^{-4}\ {\rm km}^{-2}$. These parameters are chosen such that the ratio of the isotropic radius of a TOV $0.98M_\odot$ pWD to that of a TOV $1.5M_\odot$ NS is 10:1. In addition, the EOS has been constructed so that the maximum gravitational mass of a NS is $1.8M_\odot$, i.e., the same as that for the AP2 version of the Akmal-Pandharipande-Ravenhall EOS [39,69], and the maximum gravitational mass of a pWD is $1.43M_\odot$, i.e., the maximum mass of a TOV WD obeying the Chandrasekhar EOS for mean molecular weight $\mu_e = 2$.

III. INITIAL DATA

This section introduces the formalism adopted for generating valid general relativistic initial data for binary pWDNS systems in circular orbit.

A. Gravitational field equations

The spacetime metric in the standard 3 + 1 form [70] is written as

$$ds^2 = -\alpha^2 dt^2 + \gamma_{ij}(dx^i + \beta^i dt)(dx^j + \beta^j dt), \tag{3}$$

where α is the lapse function, β^i the shift vector, and γ_{ij} the three-metric on spacelike hypersurfaces of constant time t. Throughout the paper Latin indices run from 1 to 3, and Greek indices run from 0 to 3.

The three-metric γ_{ij} is then conformally decomposed as

$$\gamma_{ij} \equiv \Psi^4 f_{ij}, \tag{4}$$

where Ψ is the conformal factor and f_{ij} the conformal metric. We adopt the standard approximation of a conformally flat spacetime, so that $f_{ij} = \delta_{ij}$ in Cartesian coordinates.

We split the extrinsic curvature (K^{ij}) into trace (K) and trace-free parts (A^{ij})

$$K^{ij} = A^{ij} + \tfrac{1}{3}\gamma^{ij} K, \tag{5}$$

take the initial slice to be maximal

$$K = 0, \tag{6}$$

and introduce a ''conformal,'' traceless extrinsic curvature as

$$\bar{A}^{ij} \equiv \Psi^{10} A^{ij}. \tag{7}$$

Using Eqs. (4)–(7) and assuming the existence of an approximate helical Killing vector, the Hamiltonian and momentum constraint equations assume the form of the conformal-thin-sandwich (CTS) equations [11]. The Hamiltonian constraint becomes

$$\bar{\nabla}^2 \Psi = -\tfrac{1}{8}\Psi^{-7} \bar{A}_{ij}\bar{A}^{ij} - 2\pi\Psi^5 \rho, \tag{8}$$

where $\bar{\nabla}^2$ is the flat Laplacian operator associated with f_{ij}. Here the source term ρ is defined as

$$\rho \equiv n^\alpha n^\beta T_{\alpha\beta}, \tag{9}$$

where n^α is the normal vector to a $t =$ constant slice, and $T_{\alpha\beta}$ is the stress-energy tensor of the matter.

The momentum constraint yields

$$\bar{\nabla}^2 \beta^i + \tfrac{1}{3}\bar{\nabla}^i(\bar{\nabla}_j \beta^j) = 2\bar{A}^{ij}\bar{\nabla}_j(\alpha\Psi^{-6}) + 16\pi\alpha\Psi^4 j^i, \tag{10}$$

where the source term j^i is given by

$$j^\alpha \equiv -\gamma^\alpha{}_\beta n_\gamma T^{\beta\gamma}. \tag{11}$$

Taking the trace of the evolution equation for K_{ij} [see Eq. (2.106) in [11]], imposing the maximal slicing condition Eq. (6), and combining the result with Eq. (8), we obtain an equation for the lapse [11]

$$\bar{\nabla}^2(\alpha\Psi) = \alpha\Psi(\tfrac{7}{8}\Psi^{-8}\bar{A}_{ij}\bar{A}^{ij} + 2\pi\Psi^4(\rho + 2S)). \quad (12)$$

Here the source term S is defined as

$$S \equiv \gamma^{ij}T_{ij}. \quad (13)$$

In all equations above

$$\bar{A}^{ij} = \frac{\Psi^6}{2\alpha}\left(\bar{\nabla}^i\beta^j + \bar{\nabla}^j\beta^i - \frac{2}{3}f^{ij}\bar{\nabla}_k\beta^k\right), \quad (14)$$

and $\bar{A}_{ij} = f_{im}f_{jn}\bar{A}^{mn}$.

Instead of solving Eq. (10) for the shift vector directly, it is convenient to decompose β^i as a sum of a vector and a gradient (cf. [71]):

$$\beta^i \equiv G^i - \tfrac{1}{4}\bar{\nabla}^i B. \quad (15)$$

Equation (10) can then be replaced by the two equivalent equations

$$\bar{\nabla}^2 G^i = 2\bar{A}^{ij}\bar{\nabla}_j(\alpha\Psi^{-6}) + 16\pi\alpha\Psi^4 j^i \quad (16)$$

and

$$\bar{\nabla}^2 B = \bar{\nabla}_i G^i. \quad (17)$$

Equations (8), (12), (16), and (17) form a system of 6 coupled, nonlinear elliptic equations for the 6 unknowns Ψ, $\alpha\Psi$, G^i, and B, which must be solved iteratively. These equations are elliptic and hence require outer boundary conditions to be specified. We impose the same fall-off boundary conditions as in [72], except that here we choose the binary components to be initially lined up on the x axis and the binary rotation axis parallel to the z axis. Table I lists the full set of outer boundary conditions imposed in our initial data.

B. Matter fields

As we argued in [34] the WD in a WDNS binary with close separation likely will be tidally locked. For this reason we focus on corotating WDNS systems only.

TABLE I. Outer boundary conditions imposed on the CTS variables when generating WDNS initial data.

Variable	Fall-off condition
$\Psi - 1$	$\sim 1/r$
$\alpha - 1$	$\sim 1/r$
G^x	$\sim y/r^3$
G^y	$\sim x/r^3$
G^z	$\sim xyz/r^7$
B	$\sim xy/r^3$

We assume that the matter is described by a perfect fluid stress-energy tensor:

$$T^{\alpha\beta} = (\rho_0 + \rho_i + P)u^\alpha u^\beta + Pg^{\alpha\beta}, \quad (18)$$

where $g^{\alpha\beta}$ is the inverse of the four-metric and ρ_0, ρ_i, P, u^α are the rest-mass density, internal energy density, pressure, and four-velocity of the fluid, respectively. For all initial configurations, the pressure is given by the cold EOS as specified in Eq. (1). The internal energy density can be derived by integrating

$$d\left(\frac{\rho_i}{\rho_0}\right) = -Pd\left(\frac{1}{\rho_0}\right), \quad (19)$$

and for Eq. (1) the integration yields

$$\frac{\rho_i}{\rho_0} = \begin{cases} n_1\kappa_1\rho_0^{1/n_1}, & \rho_0 \le \rho_1 \\ n_2\kappa_2\rho_0^{1/n_2} + c_2, & \rho_1 < \rho_0 \le \rho_2 \\ n\kappa\rho_0^{1/n_3} + c_3, & \rho_0 > \rho_2, \end{cases} \quad (20)$$

where

$$c_2 = (n_1 - n_2)\kappa_1\rho_1^{1/n_1}, \qquad c_3 = c_2 + (n_2 - n_3)\kappa_2\rho_2^{1/n_2}. \quad (21)$$

In Cartesian coordinates we choose the orbital plane of the binary to be the $z = 0$ plane, so that the fluid four-velocity takes the form [11]

$$u^\alpha = u^t(1, -\Omega y, \Omega(x - x_{\rm rot}), 0), \quad (22)$$

where Ω is the constant orbital angular velocity and $x_{\rm rot}$ is the x coordinate of the axis of rotation. Following [72], we introduce a vector

$$\xi^\alpha = (0, -y, (x - x_{\rm rot})), \quad (23)$$

and rewrite the four-velocity as

$$u^\alpha = u^t(\alpha n^\alpha + \Omega\xi^\alpha + \beta^\alpha). \quad (24)$$

The source term ρ in Eq. (9) can then be written

$$\rho = \frac{\rho_0 + \rho_i + P}{1 - \upsilon^2} - P, \quad (25)$$

where υ is the magnitude of the three-velocity of the fluid. Using $u^\alpha u_\alpha \equiv -1$, it can be shown that υ^2 is given by

$$\upsilon^2 = \frac{\Psi^4}{\alpha^2}[(\Omega y - \beta^x)^2 + (\Omega(x - x_{\rm rot}) + \beta^y)^2 + (\beta^z)^2]. \quad (26)$$

The momentum source j^i in Eq. (11) becomes

$$j^i = \frac{(\rho_0 + \rho_i + P)}{\alpha}\frac{(\Omega\xi^i + \beta^i)}{1 - \upsilon^2}, \quad (27)$$

and S in Eq. (13) is given by

$$S = (\rho_0 + \rho_i + P)\frac{\upsilon^2}{1 - \upsilon^2} + 3P. \quad (28)$$

C. Computational methods

We solve the nonlinear elliptic equations (8), (12), (16), and (17) using a fixed-mesh-refinement (FMR) finite difference code we developed, which is based on the Portable, Extensible Toolkit for Scientific Computation (PETSc) library [73–75]. A full description of our code may be found in [33]. Here we summarize the basic features.

The grid structure used in our FMR elliptic code is a multilevel set of properly nested, uniform grids. We use standard cell-centered, second-order accurate finite difference stencils for the Laplacian operator and the derivatives of the variables, using first-order interpolation across the refinement level boundaries when necessary. We calculate the solution across the entire grid, and only on leaf cells (i.e., cells within which there exist no higher resolution cells). In [33] we performed a series of tests involving single NSs, and we demonstrated that the code converges to the expected solutions at second order.

Given the matter distribution, Ω, and $x_{\rm rot}$ we solve the CTS equations iteratively, addressing the nonlinearity of Eq. (8) by performing Newton-Raphson iterations, until the residuals of all six equations become smaller than some set tolerance (usually set to 10^{-15}).

We obtain the WD rest-mass density distribution, Ω, and $x_{\rm rot}$ at the Roche limit for equilibrium, corotating binary WDNSs in circular orbit obeying our cold EOS using the unigrid Newtonian code we developed and tested in [34]. At the Roche limit, the binary separation is large enough so that the tidal effects on the NS are negligible, and hence the NS will be spherical to a high degree and pointlike from the point of view of the WD. Thus, in the Newtonian code we model the NS as a point mass and we self-consistently solve for the WD rest-mass density distribution via the integrated Euler equation. We use the Newtonian equations for this step, because it is computationally simple and fast. Also, the large separation at the Roche limit ensures that the WD and NS interaction lies in the Newtonian regime, so that our initial configuration is nearly in equilibrium.

After the WD rest-mass density distribution has been calculated, the point-mass NS is replaced by a TOV NS with gravitational mass equal to that of the point-mass NS, centered at the position of the point mass. For simplicity, we model the NS as corotational because there is no essential difference between an irrotational and a corotational NS at such large separations. The spin of a corotating NS is very small. To understand this, consider the ratio of the angular velocity of the corotating NS ($\Omega_{\rm cor}$) to that at the mass-shedding ($\Omega_{\rm ms}$) limit:

$$\frac{\Omega_{\rm cor}}{\Omega_{\rm ms}} = \sqrt{\frac{M_{\rm total}}{M_{\rm NS}}}\left(\frac{R_{\rm NS}}{A_{\rm R}}\right)^{3/2} \approx 1.3\left(\frac{R_{\rm NS}}{A_{\rm R}}\right)^{3/2}, \qquad (29)$$

where $A_{\rm R}$ is the Roche limit separation. For the typical system we consider $R_{\rm NS}/A_{\rm R} \approx R_{\rm NS}/3R_{\rm WD}$. For realistic massive WDs $R_{\rm WD}/R_{\rm NS} \approx 500$, and for pWDs $R_{\rm pWD}/R_{\rm NS} \approx 10$. Thus, $\Omega_{\rm cor}/\Omega_{\rm ms} \approx 10^{-5}$ for realistic WDNSs and $\Omega_{\rm cor}/\Omega_{\rm ms} \approx 10^{-2}$ for pWDNSs. Therefore, the corotation spin the NS acquires is very small and has no physical significance.

Having prescribed the NS and pWD rest-mass density, using second-order polynomial interpolation, we interpolate the NS and pWD matter distribution on the grid of our FMR elliptic code and solve the CTS equations.

IV. EVOLUTION OF WDNS SYSTEMS

A. Basic equations

The formulation and numerical scheme for our simulations are the same as those reported in [22,33,60,76], to which the reader may refer for details. Here we introduce our notation and summarize our method.

We use the 3 + 1 formulation of general relativity, in which the metric is decomposed as in Eq. (3). In this formalism, the fundamental dynamical variables for the metric evolution are the spatial three-metric γ_{ij} and extrinsic curvature K_{ij}. The Baumgarte-Shapiro-Shibata-Nakamura (BSSN) formalism [11,77,78] is adopted. The BSSN evolution variables are the conformal exponent $\phi \equiv \ln(\gamma)/12$, the conformal 3-metric $\tilde{\gamma}_{ij} = e^{-4\phi}\gamma_{ij}$, three auxiliary functions $\tilde{\Gamma}^i \equiv -\tilde{\gamma}^{ij}{}_{,j}$, the trace of the extrinsic curvature K, and the trace-free part of the conformal extrinsic curvature $\tilde{A}_{ij} \equiv e^{-4\phi}(K_{ij} - \gamma_{ij}K/3)$. Here $\gamma = \det(\gamma_{ij})$. The full spacetime metric $g_{\mu\nu}$ is related to the three-metric $\gamma_{\mu\nu}$ by $\gamma_{\mu\nu} = g_{\mu\nu} + n_\mu n_\nu$, where the future-directed, timelike unit vector n^μ normal to the time slice can be written in terms of the lapse α and shift β^i as $n^\mu = \alpha^{-1}(1, -\beta^i)$. The evolution equations of these BSSN variables are given by Eqs. (9)–(13) in [22].

We adopt standard puncture gauge conditions: an advective "1 + log" slicing condition for the lapse and a "Gamma-freezing" condition for the shift [79]. Thus, we have

$$\partial_0\alpha = -2\alpha K, \qquad (30)$$

$$\partial_0\beta^i = (3/4)B^i, \qquad (31)$$

$$\partial_0 B^i = \partial_0\tilde{\Gamma}^i - \eta B^i, \qquad (32)$$

where $\partial_0 \equiv \partial_t - \beta^j\partial_j$. We set the η parameter to 0.01 km^{-1} for all simulations presented in this work.

The fundamental matter variables are the rest-mass density ρ_0, specific internal energy ϵ, pressure P, and four-velocity u^μ. We write the stress-energy tensor as

$$T_{\mu\nu} = \rho_0 h u_\mu u_\nu + P g_{\mu\nu}, \qquad (33)$$

where $h = 1 + \epsilon + P/\rho_0$ is the specific enthalpy and ϵ is the specific internal energy. In our numerical implementation of the hydrodynamics equations, we evolve the following "conservative" variables:

$$\rho_* \equiv -\sqrt{\gamma}\rho_0 n_\mu u^\mu, \qquad (34)$$

$$\tilde{S}_i \equiv -\sqrt{\gamma} T_{\mu\nu} n^\mu \gamma^\nu{}_i, \tag{35}$$

$$\tilde{\tau} \equiv \sqrt{\gamma} T_{\mu\nu} n^\mu n^\nu - \rho_*. \tag{36}$$

The evolution equations for these variables are given by Eqs. (27)–(29) in [60].

The EOS we adopt for the evolution has both a thermal and cold contribution, and can therefore be written

$$P = P_{\rm th} + P_{\rm cold}, \tag{37}$$

where $P_{\rm cold}$ is given by Eq. (1) and the thermal pressure is given by

$$P_{\rm th} = (\Gamma_{\rm th} - 1)\rho_0(\epsilon - \epsilon_{\rm cold}), \tag{38}$$

where

$$\epsilon_{\rm cold} = -\int P_{\rm cold} d(1/\rho_0). \tag{39}$$

We set $\Gamma_{\rm th} = 1.66$ ($\simeq 5/3$) in all our simulations. That is, we set $\Gamma_{\rm th}$ to the Γ_1 exponent of the 10:1 EOS, appropriate either for nonrelativistic cold, degenerate electrons or (shock) heated, ideal nondegenerate baryons. Equation (37) reduces to our piecewise polytropic law Eq. (1) for the initial (cold) NS and pWD matter.

B. Evolution of the metric and hydrodynamics

We evolve the BSSN equations using fourth-order accurate, cell-centered finite-differencing stencils, except on shift advection terms, where fourth-order accurate upwind stencils are applied. We apply Sommerfeld outgoing wave boundary conditions on all BSSN fields, as in [22]. Our code is embedded in the Cactus parallelization framework [80], and our fourth-order Runge-Kutta time stepping is managed by the MOL (Method of Lines) thorn, with the Courant-Friedrichs-Lewy number set to 0.45 in all pWDNS simulations. We use the Carpet [81] infrastructure to implement the moving-box adaptive mesh refinement. In all AMR simulations presented here, we use second-order temporal prolongation, coupled with fifth-order spatial prolongation, and impose equatorial symmetry to reduce the computational cost.

We write the general relativistic hydrodynamics equations in conservative form. They are evolved via a high-resolution shock-capturing technique [60,76] that employs the piecewise parabolic (PPM) reconstruction scheme [82], coupled to the Harten, Lax, and van Leer approximate Riemman solver [83]. The adopted hydrodynamic scheme is second-order accurate. To stabilize our hydrodynamic scheme in regions where there is no matter, a tenuous atmosphere is maintained on our grid, with a density floor $\rho_{\rm atm}$ set to 10^{-10} times the initial maximum density on our grid. The average density of the pWD is 10^{11} gr/cm^3, and at least 6 orders of magnitude larger than that of the artificial atmosphere. Thus, the atmosphere poses no problem in evolving the pWD. The initial atmospheric pressure $P_{\rm atm}$ is set by using the cold EOS (1). Throughout the evolution, we impose limits on the pressure to prevent spurious heating and negative values of the internal energy ϵ. Specifically, we require $P_{\rm min} \le P \le P_{\rm max}$, where $P_{\rm max} = 10P_{\rm cold}$ and $P_{\rm min} = 0.8P_{\rm cold}$, where $P_{\rm cold}$ is the pressure calculated using the cold EOS (1). Whenever P exceeds $P_{\rm max}$ or drops below $P_{\rm min}$, we reset P to $P_{\rm max}$ or $P_{\rm min}$, respectively. Following [23] we impose the upper pressure limits only in regions where the rest-mass density remains very low ($\rho_0 < 100\rho_{\rm atm}$), but we impose the lower limit everywhere on our grid. We impose the pressure floor everywhere, because numerical error sometimes leads $\epsilon - \epsilon_{\rm cold}$ slightly below zero, resulting in negative thermal pressure. We have found experimentally that if this situation arises, it can be avoided in the subsequent time steps by imposing the pressure floor.

At each time step, the "primitive variables" ρ_0, P, and v^i must be recovered from the conservative variables ρ_*, $\tilde{\tau}$, and $\tilde{S}_i$. We perform the inversion numerically as specified in [60]. We use the same technique as in [84,85] to ensure that the values of $\tilde{S}_i$ and $\tilde{\tau}$ yield physically valid primitive variables.

C. Diagnostics

During the evolution, we monitor the normalized Hamiltonian and momentum constraints as defined in Eqs. (40)–(43) of [22]. We also monitor the Arnowitt-Deser-Misner (ADM) mass and angular momentum of the system. The equations used to calculate the ADM mass and angular momentum with minimal numerical noise are as follows [11]:

$$M = \int d^3x \Big(\psi^5 \rho + \frac{1}{16\pi} \psi^5 \tilde{A}_{ij} \tilde{A}^{ij} - \frac{1}{16\pi} \tilde{\Gamma}^{ijk} \tilde{\Gamma}_{jik} + \frac{1-\psi}{16\pi} \tilde{R} - \frac{1}{24\pi} \psi^5 K^2 \Big), \tag{40}$$

$$J_i = \frac{1}{8\pi} \epsilon_{ij}{}^n \int d^3x \Big[\psi^6 \Big(\tilde{A}^j{}_n + \frac{2}{3} x^j \partial_n K - \frac{1}{2} x^j \tilde{A}_{km} \partial_n \tilde{\gamma}^{km} \Big) + 8\pi x^j S_n \Big]. \tag{41}$$

Here $\psi = e^\phi$, $\rho = n_\mu n_\nu T^{\mu\nu}$, $S_i = -n_\mu \gamma_{i\nu} T^{\mu\nu}$, $\tilde{R}$ is the Ricci scalar associated with $\tilde{\gamma}_{ij}$, and $\tilde{\Gamma}_{ijk}$ are Christoffel symbols associated with $\tilde{\gamma}_{ij}$.

When hydrodynamic matter is evolved on a fixed uniform grid, our hydrodynamic scheme guarantees that the rest mass M_0 is conserved to machine round-off error. This strict conservation is no longer maintained in an AMR grid, where spatial and temporal prolongation is performed at the refinement boundaries. Hence, we also monitor the rest mass

$$M_0 = \int \rho_* d^3x \tag{42}$$

during the evolution. Rest-mass conservation is also violated whenever ρ_0 is reset to the atmosphere value. This usually happens only in the very low-density atmosphere. The low-density regions do not affect rest-mass conservation significantly.

In all simulations we present in this work the normalized Hamiltonian constraint violations remain smaller than 0.9% and the normalized momentum constraint violations smaller than 2.1%. Rest mass is conserved to within 4% and angular momentum to within 10%.

Shocks occur when the stars collide. We measure the entropy generated by shocks via the quantity $K \equiv P/P_{\rm cold} \geq 1$, where $P_{\rm cold}$ is the pressure associated with the cold EOS that characterizes the initial matter [see Eq. (1)].

V. RADIATIVE COOLING

Our binary WDNS head-on collision studies in [33] demonstrate that the hot, quasiequilibrium TZlO remnants do not collapse promptly to a black hole, even though the final total mass is larger than the maximum mass supportable by the cold EOS. This outcome might also arise in the case of WDNS mergers in circular orbit, and can be due to additional support provided by thermal pressure and/or rapid rotation. In order to determine whether thermal support is dominant, we add radiative cooling to the GR hydrodynamic equations. We now describe our formalism for implementing this.

The dynamics of radiation is governed by [86–88]

$$\nabla_\alpha R^{\alpha\beta} = -G^\beta, \tag{43}$$

where $R^{\alpha\beta}$ is the radiation stress-energy tensor given by

$$R^{\alpha\beta} = \int d\nu d\Omega I_\nu N^\alpha N^\beta, \tag{44}$$

and G^α is the radiation four-force density given by

$$G^\alpha = \int d\nu d\Omega (\chi_\nu I_\nu - j_\nu) N^\alpha. \tag{45}$$

In the equations above $d\Omega$ is the solid angle; ν and $I_\nu = I_\nu(x^\alpha, N^i, \nu)$ are the radiation frequency and specific intensity of radiation at x^α moving in direction $N^\alpha = p^\alpha/h\nu$, respectively. All quantities are measured in the local Lorentz frame of a fiducial observer with four-velocity $u^\alpha_{\rm fid}$, i.e.,

$$h\nu = -p_\alpha u^\alpha_{\rm fid}, \tag{46}$$

where p^α is the photon four-momentum and h denotes Planck's constant. The energy-momentum conservation equation then becomes

$$\nabla_\alpha (T^{\alpha\beta} + R^{\alpha\beta}) = 0 \tag{47}$$

or after using Eq. (43)

$$\nabla_\alpha T^{\alpha\beta} = G^\beta. \tag{48}$$

After projecting this equation using the fluid four-velocity u^α, we obtain the modified energy equation:

$$u^\alpha \nabla_\alpha \varepsilon = -(\varepsilon + P)\nabla_\alpha u^\alpha - u^\alpha G_\alpha, \tag{49}$$

where the perfect fluid stress-energy tensor has been written as

$$T^{\mu\nu} = (\varepsilon + P)u^\mu u^\nu + P g^{\mu\nu}, \tag{50}$$

and ε is the total energy density. Using the continuity equation

$$\nabla_\alpha (\rho_0 u^\alpha) = 0, \tag{51}$$

Eq. (49) becomes

$$u^\alpha \nabla_\alpha \varepsilon = \frac{\varepsilon + P}{\rho_0} u^\alpha \nabla_\alpha \rho_0 - u^\alpha G_\alpha. \tag{52}$$

The total energy density is related to the specific thermal energy via the following equation:

$$\varepsilon = \rho_0 (1 + \epsilon_{\rm th} + \epsilon_{\rm cold}). \tag{53}$$

Using Eqs. (52) and (53) we find that the specific thermal energy evolves as

$$u^\alpha \nabla_\alpha \epsilon_{\rm th} = \frac{P_{\rm th}}{\rho_0^2} u^\alpha \nabla_\alpha \rho_0 - \frac{1}{\rho_0} u^\alpha G_\alpha, \tag{54}$$

where we have used $d\epsilon_{\rm cold}/d\rho_0 = P_{\rm cold}/\rho_0^2$, and $P_{\rm th} = P - P_{\rm cold}$.

In the comoving reference frame $u^\alpha \nabla_\alpha = d/d\tau$, where τ is the proper time. Thus, in the comoving frame Eq. (54) becomes

$$\frac{d}{d\tau}\epsilon_{\rm th} = \frac{P_{\rm th}}{\rho_0^2}\frac{d}{d\tau}\rho_0 - \frac{1}{\rho_0} u^\alpha G_\alpha. \tag{55}$$

In order to achieve cooling, the radiation term in (55) must be specified so that thermal energy can be removed. For this reason we choose the following cooling law that gives rise to exponential cooling:

$$u^\alpha G_\alpha = \epsilon_{\rm th}\rho_0/\tau_c, \tag{56}$$

where $\tau_c > 0$ is the cooling time scale. Substituting Eq. (56) in Eq. (55) we obtain

$$\frac{d}{d\tau}\epsilon_{\rm th} = \left[\frac{(\Gamma_{\rm th} - 1)}{\rho_0}\frac{d\rho_0}{d\tau} - \frac{1}{\tau_c}\right]\epsilon_{\rm th}, \tag{57}$$

where we used Eq. (38) to substitute for the thermal pressure.

The first term in brackets on the right-hand side of Eq. (57) results from adiabatic compression or expansion. The second term results from cooling and radiates away thermal energy exponentially. Thus, if initially we have a quasiequilibrium spherical object which is thermally supported, and we cool it quasistatically, i.e., choose a cooling time scale much longer than the free-fall time scale of the star, it will radiate thermal energy away and contract. While the contraction generates extra heat, radiation tends

to remove any residual thermal energy. Thus, after cooling, TZlOs are expected either to collapse to a BH or to be supported by the residual cold pressure and centrifugal force.

In the optically thin regime, assuming the fluid radiates isotropically in its rest frame, and using $u^\alpha_{\rm fid} = u^\alpha$, the source term G^α is generally expressed as [87,88]

$$G^\alpha = u^\alpha(\Gamma - \Lambda) + \int d\nu(\chi^a_\nu + \chi^s_\nu)F^\alpha_\nu, \qquad (58)$$

where Γ and Λ are the heating and cooling terms, respectively, given by

$$\Gamma = \int d\nu d\Omega \chi^a_\nu I_\nu, \qquad \Lambda = \int d\nu d\Omega j_\nu, \qquad (59)$$

and where χ^a_ν, χ^s_ν are the absorption and scattering coefficients, respectively, and j_ν is the emissivity. Finally, F^α_ν is the total radiation flux four-vector

$$F^\alpha_\nu = P^\alpha{}_\beta \int d\Omega I_\nu N^\beta, \qquad (60)$$

where the projection operator $P^\alpha{}_\beta$ is defined as

$$P^\alpha{}_\beta \equiv \delta^\alpha{}_\beta + u^\alpha u_\beta. \qquad (61)$$

If we assume that there is no absorption and no scattering, Eq. (58) becomes

$$G^\alpha = -u^\alpha \Lambda. \qquad (62)$$

As a result,

$$u_\alpha G^\alpha = \Lambda. \qquad (63)$$

A straightforward comparison of Eqs. (56) and (63) shows that the integrated emissivity in our cooling model is given by

$$\Lambda = \frac{\rho_0}{\tau_c}\epsilon_{\rm th}. \qquad (64)$$

If we project Eq. (48) using the timelike unit vector n^α normal to spacelike hypersurfaces and the projection operator $h^\alpha{}_\beta = \delta^\alpha{}_\beta + n^\alpha n_\beta$, we find that the 3 + 1 general relativistic hydrodynamic equations become

$$\partial_t \tilde{S}_i + \partial_j(\alpha\sqrt{\gamma}T^j{}_i) = \tfrac{1}{2}\alpha\sqrt{\gamma}T^{\alpha\beta}g_{\alpha\beta,i} - \alpha\sqrt{\gamma}u_i\Lambda, \quad (65)$$

and

$$\partial_t \tilde{\tau} + \partial_i(\alpha^2\sqrt{\gamma}T^{0i} - \rho_* v^i) = s - \alpha^2\sqrt{\gamma}u^0\Lambda, \qquad (66)$$

where we have used Eq. (62) and Λ is given by Eq. (64). Thus, cooling enters as a source term in the general relativistic hydrodynamic equations, which is precisely how cooling is implemented in our high-resolution shock-capturing code.

Note that the optically thin approximation employed here is valid for neutrino cooling in the WDNS merger scenario (head-on or otherwise). According to our analysis in [33], the temperatures and densities of the hot mantle of a TZlO are such that thermal neutrino emission likely will be the dominant source of cooling. The diffuse TZlO mantle composed of the WD debris is optically thin to neutrinos, justifying the above approximation.

Finally, note that the self-gravity of the radiation is neglected; i.e., we assume that radiation does not affect the spacetime structure, so only the perfect fluid stress-energy tensor contributes to the BSSN source terms. This is a good approximation as long as the radiation energy density is subdominant ($n_\alpha n_\beta R^{\alpha\beta} \ll n_\alpha n_\beta T^{\alpha\beta}$). This is indeed the case in a WDNS scenario because the rest mass dominates the mass energy as can be inferred by the local constraint violations. In addition, the NS (i.e., the most compact object in our scenario) remains almost unaffected and cold throughout the evolution; i.e., radiation has no effect on the spacetime structure in the vicinity of the NS. In all simulations we present here for radii (r) such that $r \gtrsim R_{\rm core} \approx 20$ km, the local constraint violations remain smaller than 0.1% throughout the evolution after cooling is turned on, justifying our neglecting of the radiation self-gravity.

VI. COOLING OF TZLOS FORMED IN HEAD-ON COLLISIONS

We found in [33] that all our binary pWDNS head-on collisions formed hot, quasiequilibrium TZlOs, which were more massive than the maximum mass our cold EOS can support. However, these remnants did not collapse promptly to a black hole. As there is no angular momentum involved in a head-on collision, the additional support that prevents collapse arises from thermal pressure alone. Therefore, if one were to cool these objects, one would expect that they would eventually collapse on a cooling time scale. We check this expectation here so that we may implement the same cooling mechanism in the inspiral case, where the outcome is not so certain.

To determine the dominant cooling mechanism, and hence the cooling time scale, one needs to know the density and temperature of the matter. We estimated the temperature of realistic TZlOs to be of order 10^9 K. Given that typical WD densities are of order 10^6 g/cm^3, it is likely that cooling will be dominated by thermal neutrino processes. Realistic neutrino cooling time scales are at best of order 1 yr (see discussion in Sec. VIII), or equivalently $\sim 10^7$ TZlO dynamical time scales. This slow cooling rate ensures that the collapse of TZlOs will be quasistatic. However, realistic cooling time scales are so long that it would be impossible to follow this secular phase with hydrodynamic simulations in full GR because of the prohibitive computational cost.

Nevertheless, to confirm that these TZlOs collapse to BHs after they have cooled, we can simply scale up the cooling law, as long as we keep the cooling time scale longer than the hydrodynamical time scale.

We can estimate the dynamical time scale of a TZlO as

$$t_{\rm TZlO} = \sqrt{\frac{R^3_{\rm TZlO}}{M_{\rm TZlO}}}, \tag{67}$$

where $R_{\rm TZlO}$ and $M_{\rm TZlO}$ are the radius and mass of the remnant, respectively. Here we define the radius of TZlOs by the radius of a coordinate sphere that contains 90% of the remnant's total mass. For case A1 we find $t_{\rm TZlO} \approx 2300$ km ≈ 654.5 M. The TZlO dynamical time scale in case A3 is approximately the same as that of case A1. We choose $\tau_c = 6000$ km for both cases, so that initially $\tau_c \approx 2.6 t_{\rm TZlO}$. This way we reduce the simulation time, while maintaining the time-scale inequality.

Though we choose τ_c to be only a few times $t_{\rm TZlO}$, it is $\gtrsim 100$ times larger than the dynamical time scale ($t_{\rm core}$) of the innermost, cold, NS core, which satisfies $t_{\rm core}/t_{\rm TZlO} \sim 15^{3/2} \approx 60$. This property is important because the core of the TZlO collapses first. Finally, note that as the entire remnant contracts, its dynamical time scale decreases so that the required inequalities are better satisfied with increasing time.

Our expectation is that these TZlOs will collapse following cooling and that collapse should occur on a cooling time scale. Given that (a) the shock-induced thermal energy is comparable to the gravitational binding energy, and (b) the total remnant mass is close to the maximum mass of a cold configuration allowed by our adopted EOS, we also expect that a large fraction of the thermal energy needs to be removed to induce collapse. Note that this expectation applies solely to TZlOs formed in head-on collisions. When TZlOs form after the merger of WDNSs in an initially circular orbit, the remnant rotates. Hence, we cannot tell *a priori* that collapse will take place because of the additional centrifugal support.

Table II summarizes the physical parameters of the head-on collision cases we study, and Table III presents the AMR grid structure used in each case. All our simulations with cooling turned on show that the TZlOs remnants formed in the head-on collisions begin to contract, and within a few cooling time scales collapse to a black hole. In contrast, we find that when cooling is turned off the remnant does not collapse and remains in quasiequilibrium. All these results can be clearly seen in Figs. 1 and 2, which correspond to case A1. Case A3 is qualitatively similar.

In Fig. 1 rest-mass density contours are plotted in the orbital plane at selected times. Figure 2 shows the

TABLE II. Summary of initial configurations. $M_{\rm NS}$ ($M_{\rm WD}$) is the ADM mass of an isolated NS (pWD)[a], $R_{\rm NS}$ ($R_{\rm WD}$) the isotropic radius of an isolated NS (pWD), and $C_{\rm NS}$ the compaction of an isolated NS, where the compaction is the ratio of the ADM mass of the isolated star to its areal radius. All pWDs considered here have $C_{\rm WD} = 0.01$. $M_{\rm ADM}$ is the ADM mass of the system and A the initial binary separation in isotropic coordinates. Cases A1 and A3 are the same as the head-on collision cases we studied in [33]. The initial coordinate separation for these cases was set to 587 km. Case A corresponds to our simulation of a binary pWDNS in circular orbit starting at the Roche limit. For this case $\Omega M_{\rm ADM} = 6.95 \times 10^{-4}$. All cases have been produced with the 10:1 EOS of [33].

Case	$M_{\rm NS}/M_\odot$	$M_{\rm WD}/M_\odot$	$C_{\rm NS}$	$J/M^2_{\rm ADM}$	$R_{\rm WD}/R_{\rm NS}$	$R_{\rm WD}/M_{\rm ADM}$	$M_{\rm ADM}/M_\odot$	$A/R_{\rm WD}$
A1	1.4	0.98	0.11	0.	8.88	41.18	2.41	4.00
A3	1.6	0.98	0.15	0.	11.15	37.46	2.65	4.00
A	1.4	0.98	0.11	2.88	8.88	40.05	2.48	3.14

[a]Here we list the ADM masses, isotropic radii, and compactions of the isolated NS stars, whose rest-mass density profiles were used to generate initial data. The same holds for the pWDs in cases A1 and A3. In case A the pWD rest-mass density profile, the Roche limit separation, and Ω were generated by a Newtonian binary WDNS code and then used in our CTS solver.

TABLE III. Grid configurations used in our simulations. Here M is the sum of the ADM masses of the isolated stars, Δx is the grid spacing in the innermost refinement box surrounding the NS, $N_{\rm NS}$ denotes the number of grid points covering the diameter of the NS initially, and $N_{\rm WD}$ denotes the number of grid points covering the (smallest) diameter of the pWD initially. The outer boundary distance to the center of mass is approximately $1020M$ in cases A1 and A3, and $540M$ in case A.

Case	$M/M_\odot$	Grid hierarchy (in units of M)[a]	Δx	$N_{\rm NS}$	$N_{\rm WD}$
A1	2.38	(534.33, 267.16, 133.58, 66.79, 35.78, 19.08, 10.44, 7.156)	$M/6.71$	63	35
A3	2.58	(467.27, 233.64, 116.82, 58.41, 29.20, 15.58, 8.518, 5.841)	$M/8.22$	56	38
A	2.38	(270.87, 135.44, 67.72, 36.28[N/A], 19.35[N/A], 9.674[N/A], 5.744[N/A])	$M/13.2$	124	73

[a]There are two sets of nested refinement boxes: one centered on the NS and one on the pWD. This column specifies the half-length of the sides of the refinement boxes centered on both the NS and pWD. When there is no corresponding pWD refinement box (as the pWD is much larger than the NS), we write [N/A] for that box.

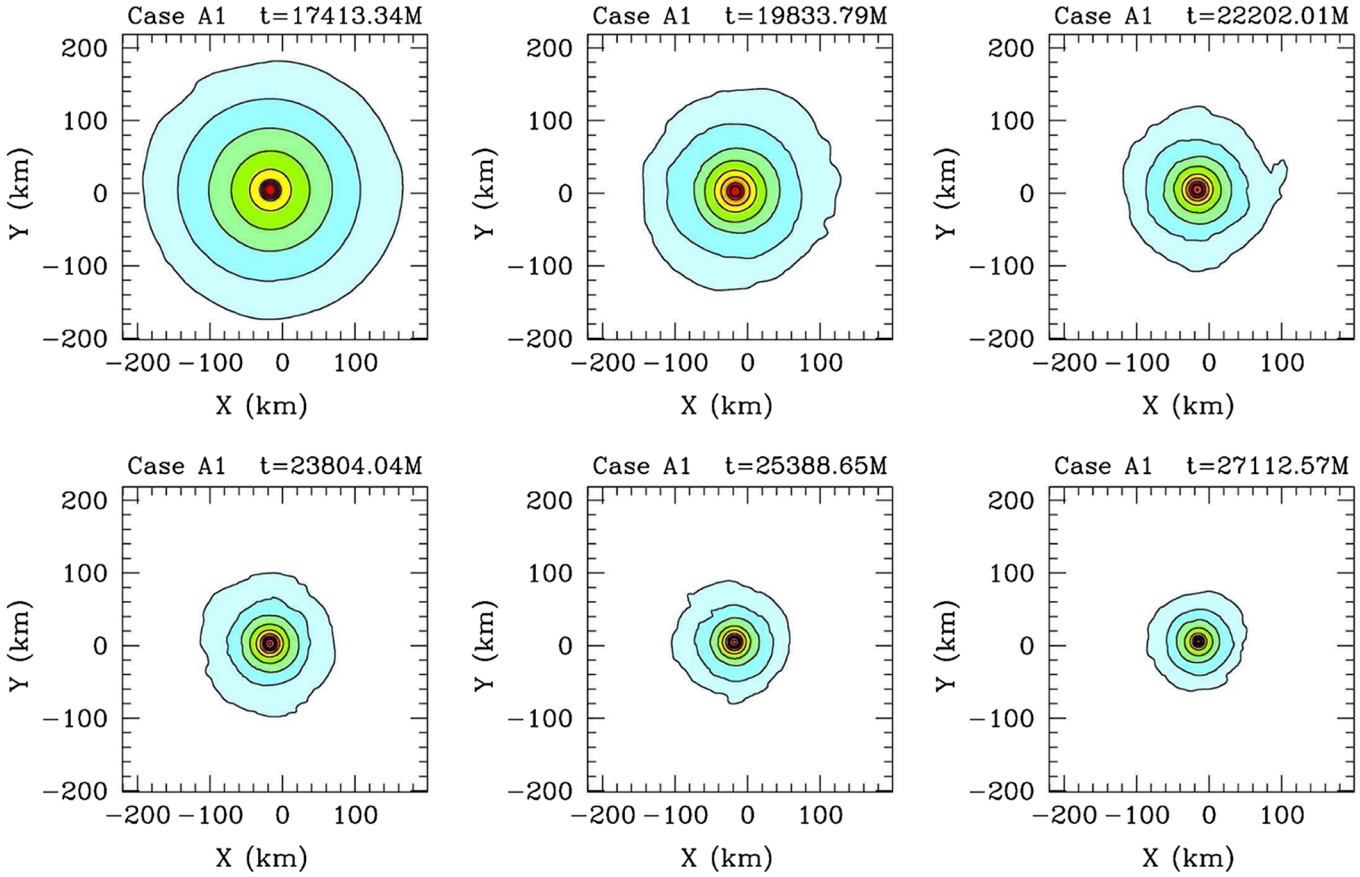

FIG. 1 (color online). Snapshots of rest-mass density profiles at selected times for head-on case A1 after cooling is turned on. The contours represent the rest-mass density in the orbital plane, plotted according to $\rho_0 = \rho_{0,\max} 10^{-0.68j-0.16} (j = 0, 1, \ldots, 7)$. The color sequence from the center outward (dark red, red, orange, yellow, green, light green, blue, and light blue) implies a sequence from higher to lower values. This roughly corresponds to a darker grey scale for higher values. Here $\rho_{0,\max} = 4.645\rho_{\rm nuc}$, where $\rho_{\rm nuc} = 2 \times 10^{14}$ g/cm^3. These snapshots clearly demonstrate that the entire TZlO remnant collapses once cooling is turned on. Here $M = 2.38 M_\odot = 3.52$ km $= 1.17 \times 10^{-5}$ s is the sum of the ADM masses of the isolated stars.

evolution of the maximum rest-mass density with and without cooling, the minimum value of the lapse function, and the rest mass contained within different radii from the center of mass. If the cooling mechanism remains off, both the maximum value of the density and the minimum value of the lapse remain constant with time (see left and middle panels of Fig. 2). We find that the same holds true for the rest mass contained within 40 km and 220 km.

By contrast, if cooling is turned on, the maximum density (minimum lapse) increases (decreases) with time. Moreover, the rest mass contained within 40 km and 220 km increases with time, indicating that the outer layers are also contracting as the TZlO cools (see right panel in Fig. 2). Initially, the maximum density (minimum lapse) increases (decreases) almost linearly with time, until $\rho_{0,\max}$ crosses the value of 2.16×10^{15} g/cm^3, which corresponds to that of a maximum-mass NS configuration built with our cold EOS. Soon after this point, the remnant essentially free-falls, the density blows up, the lapse function plummets, and a BH is eventually formed. The BH in case A1 can be seen in Fig. 3, where we plot rest-mass density contours and $K = P/P_{\rm cold}$ contours in the orbital plane in the innermost 12 km of the remnant, which contain about 85% of the total mass at the time of BH formation. The K contours show that the matter around the BH is cold, i.e., $K \approx 1$, as expected.

Cases A1 and A2 collapse to a black hole after about 5 and 3 cooling time scales, respectively, which is expected as the collapse proceeds without additional shock heating. The mass of the black hole when an apparent horizon forms for the first time is $M_{\rm BH} \approx 1.4 M_\odot$ and the coordinate radius of the BH (in our adopted gauge) is $R_{\rm BH} \approx 1.08$ km $\approx 0.53 M_{\rm BH}$. Thus we have demonstrated that our cooling mechanism yields results which are consistent with our theoretical expectations.

VII. BINARY WDNS INSPIRAL

To predict the final outcome of a binary WDNS in an initially circular orbit, we performed a simulation of a

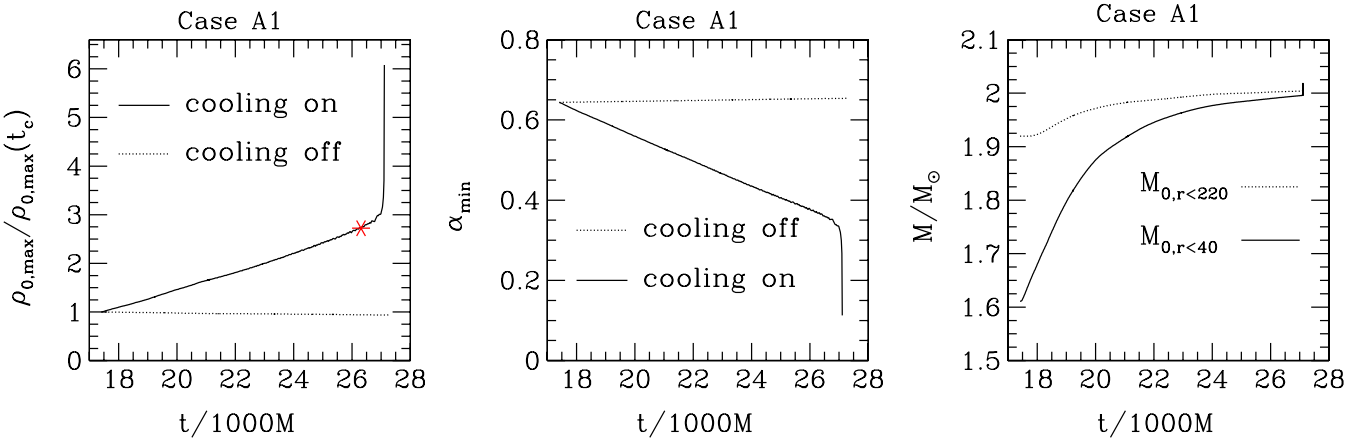

FIG. 2 (color online). Left panel: Evolution of maximum value of rest-mass density with cooling (solid curve) and without cooling (dotted curve) for the case shown in Fig. 1. Here $\rho_{0,\max}$ is the maximum value of the rest-mass density; $\rho_{0,\max}(t_c) = 5.879 \times 10^{-4}$ km^{-2} $= 7.919 \times 10^{14}$ g/cm^3 is the maximum value of rest-mass density at the time ($t_c = 17\,413M$) when cooling is turned on. The asterisk on the curve denotes the value of the central density corresponding to the maximum-mass TOV NS ($\rho_{\max,\mathrm{TOV}} = 2.16 \times 10^{15}$ g/cm^3). Soon after the maximum density of the TZlO crosses $\rho_{\max,\mathrm{TOV}}$, the remnant collapses to a BH. Middle panel: Evolution of minimum value of the lapse function ($\alpha_{\min}$) with cooling (solid curve) and without cooling (dotted curve). Right panel: Evolution of rest mass contained within different radii with cooling turned on. Here $M_{0,r<r_0}$ stands for the rest mass contained within a coordinate sphere of radius r_0 in units of km, centered on the remnant's center of mass. These plots demonstrate that the TZlO remnant collapses as a whole. All plots correspond to case A1, and $M = 2.38M_\odot = 3.52$ km $= 1.17 \times 10^{-5}$ s.

corotating binary pWDNS starting at the Roche limit separation. Throughout, we label this case by the letter A. Table II outlines the physical parameters of case A, and Table III outlines the adopted AMR grid structure.

For the simulations performed here, we were able to demonstrate 2nd-order convergence for the first quarter of an orbit monitoring the conservation of angular momentum, and the constraint violations. The convergence study

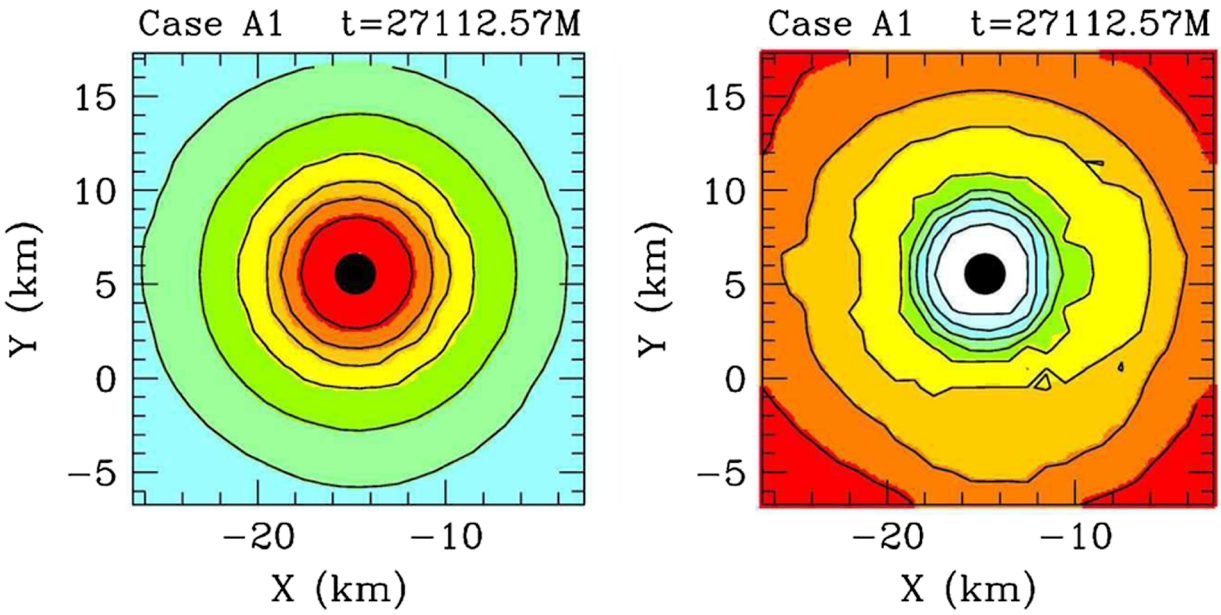

FIG. 3 (color online). Left: Snapshot of rest-mass density profile at the end of the A1 simulation shown in Fig. 1. Contours represent the rest-mass density in the orbital plane, plotted according to $\rho_0 = \rho_{0,\max} 10^{-0.5j-0.088}$ ($j = 0, 1, \ldots, 7$). Here $\rho_{0,\max} = 4.645\rho_{\mathrm{nuc}}$, where $\rho_{\mathrm{nuc}} = 2 \times 10^{14}$ g/cm^3. Right: Snapshot of $K = P/P_{\mathrm{cold}}$ profile at the end of the A1 simulation. The contours represent K in the orbital plane, plotted according to $K = 10^{-0.1125j+0.9}$ ($j = 0, 1, \ldots, 7$). The plot demonstrates that the matter near the BH is cold ($K \approx 1$), as expected, and K increases with the distance from the core. The color coding is the same as that used in Fig. 1, with white indicating $K \approx 1$. The black disk in the center denotes the BH apparent horizon. The plots focus in the innermost 12 km from the TZlO center of mass, where the object is approximately spherical, and for this reason we do not show XZ and YZ meridional slices. Here $M = 2.38M_\odot = 3.52$ km $= 1.17 \times 10^{-5}$ s is the sum of the ADM masses of the isolated stars.

showed that angular momentum decays linearly with time, but the linear decay rate decreases with increasing resolution to second order. Moreover, this decay rate remains roughly constant up until merger. Furthermore, a resolution study using pWDNSs systems has been carried out in [33], where we showed that the results were qualitatively insensitive to resolution implying that the resolutions used were sufficiently high. The resolution used in our inspiral pWDNS calculations is twice that used in [33] indicating that our simulations are well within the convergent regime.

A. Initial configuration

We prepared valid general relativistic initial data as described in Sec. III. The ADM masses of the compact objects in isolation we consider are $0.98M_\odot$ and $1.4M_\odot$ for the pWD and NS, respectively. After solving the CTS equations, we map ρ_0, Ψ and α, β^i, and v^i, from the grids used in the elliptic solver code onto the grids used in the evolution code via second-order polynomial interpolation. For accuracy, we make sure that the resolution of the initial data grids is always higher than the resolution of the evolution grids.

B. Dynamics of the WDNS merger

In [34] we analyzed the stability of corotating binary WDNSs at the Roche limit, accounting for GR effects on the mass-radius relationship of the WD. We concluded that if the mass ratio $q = M_{\rm WD}/M_{\rm NS}$ is larger than a critical mass ratio $q_{\rm crit} \approx 0.5$, then mass transfer from the WD to the NS will be unstable, and the WD will be tidally disrupted. The binary pWDNS system simulated in this work has a mass ratio $q = 0.7$, so we expect that the system should experience tidal disruption and merge on an orbital time scale soon after mass transfer has started.

In our simulations, the pWDNS binary completes almost 2.5 orbits before the pWD is completely disrupted. Figure 4 plots rest-mass density contours in the orbital plane at selected times for case A. The top row, middle panel shows the binary shortly after completing the first orbit. At this

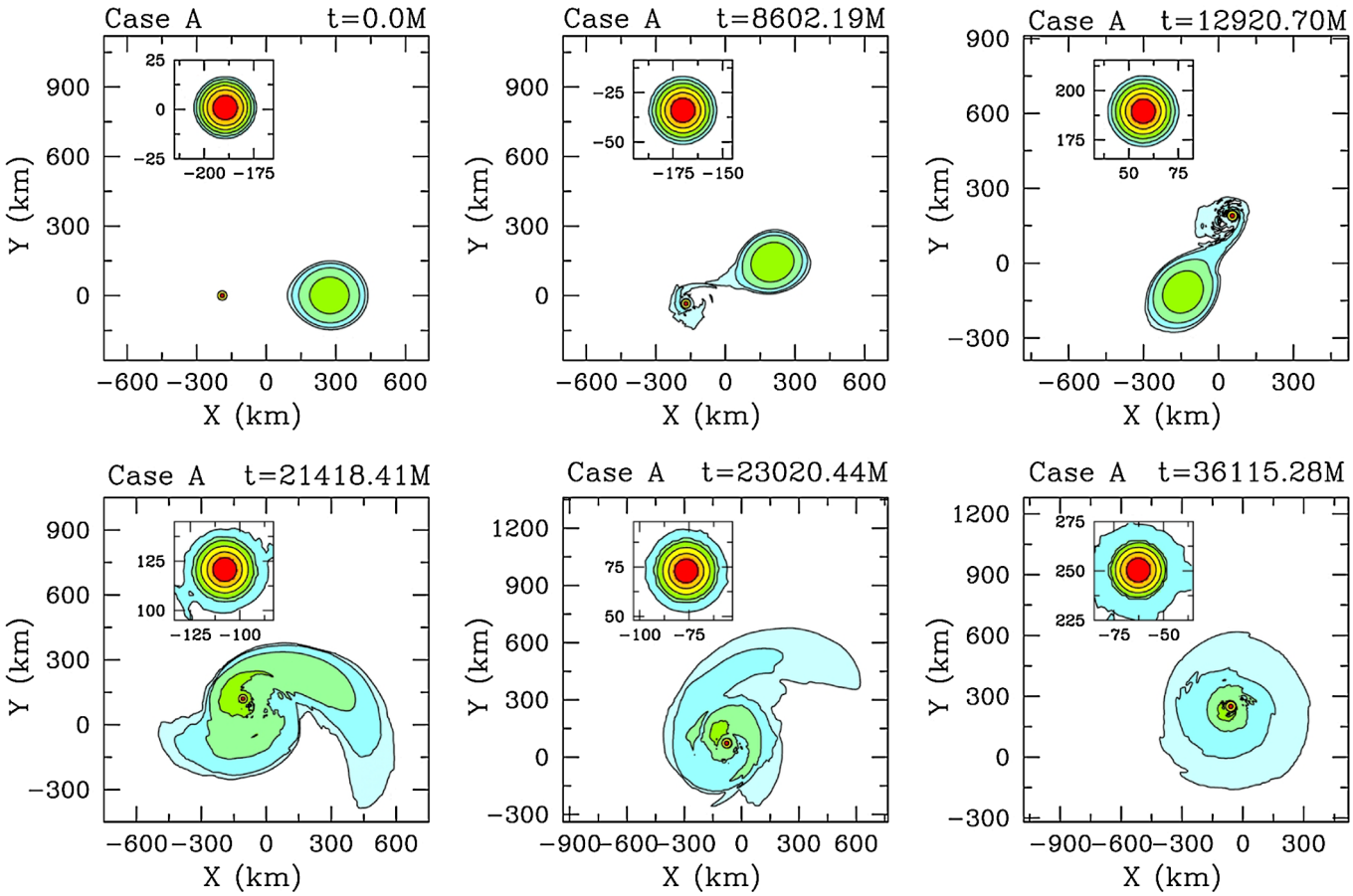

FIG. 4 (color online). Snapshots of rest-mass density profiles at selected times for case A. The contours represent the rest-mass density in the orbital plane, plotted according to $\rho_0 = \rho_{0,\rm max} 10^{-0.66j-0.16} (j = 0, 1, \ldots, 9)$. The insets focus on the NS and demonstrate it is nearly unaffected by the merger. The inset density contours are plotted according to $\rho_0 = \rho_{0,\rm max} 10^{-0.525j-0.861} (j = 0, 1, \ldots, 7)$. In both cases $\rho_{0,\rm max} = 4.645\rho_{\rm nuc}$, where $\rho_{\rm nuc} = 2 \times 10^{14}$ g/cm^3. The color coding is the same as that used in Fig. 1, with white indicating near vacuum. Here $M = 2.38M_\odot = 3.52$ km $= 1.17 \times 10^{-5}$ s is the sum of the ADM masses of the isolated stars.

time, an accretion stream from the pWD to the NS develops, followed by the formation of an accretion disk around the NS. Matter from the accretion stream smashes into the accretion disk, shock heating the gas at that location. This process continues until the pWD is completely disrupted. After pWD tidal disruption, a long tail forms that moves outwards and around the NS. The pWD matter that orbits the NS at closer separations collides with the tail inducing further strong shocks.

The bottom row, left panel of Fig. 4 shows the system after 3 orbits have been completed. At this point, the pWD is completely disrupted and a large, rotating, massive mantle and disk around the NS has begun to form. A tidal tail is also visible. This snapshot is followed by a long epoch in which the rotating mantle settles onto an extended disk around the central object, composed of a slowly spinning, cold NS core surrounded by a hot atmosphere and disk composed of pWD debris. We find that even at this late stage, the NS core maintains its original spin, and the hot mantle surrounding it spins and settles into quasiequilibrium. Nonaxisymmetric clumps of matter inspiraling near the cold NS core launch spiral density waves into the disk. The remnant of the pWDNS merger may be best characterized as a spinning TZlO with an extended ($R_{\rm disk} \sim 1000$ km), massive disk.

We define the radius of the TZlO ($R_{\rm TZlO}$) as the distance between the center of mass and the ''north'' pole of the remnant. The z radius of the remnant for a cutoff density $\sim 10^{-8}\rho_{0,\rm max}$, where $\rho_{0,\rm max}$ is the maximum density of the remnant, is $R_{\rm TZlO} \approx 300$ km. We estimate the rest mass of the TZlO ($M_{\rm TZlO}$) as the rest mass contained within a sphere of coordinate radius equal to $R_{\rm TZlO}$, and the disk mass ($M_{\rm disk}$) by subtracting $M_{\rm TZlO}$ from the total rest mass. We find $M_{\rm TZlO} = 1.82M_\odot$ and $M_{\rm disk} = 0.7M_\odot$. The disk is massive and $\gtrsim 50\%$ of the original WD rest mass is eventually stored in the disk.

To first order, the TZlO is spherical. This is evidenced by the XY, XZ, and YZ density contour plots of Fig. 5, which focus on the innermost regions of the remnant at the end of the simulation.

The cutoff density in all the density contour plots we show here is $10^{-8.5}$ km$^{-2} \approx 10^{-5.3}\rho_{0,\rm max}$, which is approximately 4 decades above atmosphere density. The equatorial and polar coordinate radii of these contours are $r_e \approx 350$ km and $r_p \approx 150$ km, respectively. Therefore, the ratio of these radii is $r_p/r_e \approx 3/7$. Given that the core of the remnant is approximately spherical, the smallness of the ratio r_p/r_e indicates that the disk stores a large amount of angular momentum.

In the bottom row of Fig. 5, we plot contours of $K = P/P_{\rm cold}$. These entropy contours show that the neutron star core is cold $K \approx 1$ and that K increases with the distance from the core in the orbital plane and with increasing z in meridional planes. This is reminiscent of the K pattern observed in our binary pWDNS head-on collision studies in [33], where $K \approx 1$ in the core, but increases with distance from the center. Note the spiral density wave pattern visible in the bottom row, left panel of Fig. 5.

Unlike the head-on collision case, in which the outermost layers of the NS are shock heated and stripped away when the NS smashes into the denser parts of the pWD (Fig. 4 insets, [33]), after a pWDNS binary inspiral and merger, the NS retains its outer layers, and its structure remains nearly unaffected throughout the simulation (Fig. 4 insets). Moreover, in the head-on collision, about 18% of the total initial rest mass is ejected to infinity, but in the inspiral case, no ejection of matter to infinity is observed.

As in the case of head-on collisions, we find that the typical temperature in our inspiraling binary remnant is of order 10^{11} K. In Fig. 6 we show temperature profiles of the remnant. To estimate the temperature T, we assume that the temperature dependence of $\epsilon_{\rm th}$ can be modeled as

$$\epsilon_{\rm th} = \frac{3k\mathrm{T}}{2m_n} + f\frac{a\mathrm{T}^4}{\rho_0}, \tag{68}$$

where m_n is the mass of a nucleon, k is Boltzmann's constant, and a is the radiation constant. The first term represents the approximate thermal energy of the nucleons, and the second term accounts for the thermal energy due to relativistic particles. The factor f reflects the number of species of relativistic particles that contribute to the thermal energy. When $\mathrm{T} \ll 2m_e/k \sim 10^{10}$ K, where m_e is the electron mass, thermal radiation is dominated by photons and $f = 1$. When $\mathrm{T} \gg 2m_e/k$, electrons and positrons become relativistic and also contribute to radiation, and $f = 1 + 2 \times (7/8) = 11/4$. At sufficiently high temperatures and densities ($\mathrm{T} \gtrsim 10^{11}$ K, $\rho_0 \gtrsim 10^{12}$ g cm^{-3}), neutrinos are generated copiously and become trapped. So, taking into account three flavors of neutrinos and antineutrinos, $f = 11/4 + 6 \times (7/8) = 8$. In our temperature estimate, we find f self-consistently in the following sense: we first calculate the temperature assuming $f = 0$. If the calculated temperature and density are inconsistent with our choice of f (which we test based on the above inequalities), then we choose a different f, until we find the value of f which is consistent. We find that $f = 11/4$ is consistent with the temperatures and densities in our pWDNS merger. However, we expect that in realistic mergers $f = 1$, as the expected temperatures are of order 10^9 K [see discussion following Eq. (71)].

To solve Eq. (68) for T we need to know $\epsilon_{\rm th}$. We calculate $\epsilon_{\rm th}$ via

$$\epsilon_{\rm th} = \frac{(K-1)P_{\rm cold}}{(\Gamma_{\rm th}-1)\rho_0}, \tag{69}$$

where Eqs. (37) and (38) and the definition of K were used to obtain this last equation.

As in our pWDNS head-on collision studies, we find that the pWDNS binary remnant does not collapse promptly to a BH. In contrast to the head-on collision cases, in which only thermal pressure supported the remnant from prompt collapse, collapse *may* be delayed in the pWDNS binary inspiral case by both thermal pressure and centrifugal support. One way to assess the importance of thermal support in the binary inspiral remnant is to apply the same cooling recipe as in the case of TZlOs formed in head-on collisions (see Sec. VI), and compare the result to an uncooled case.

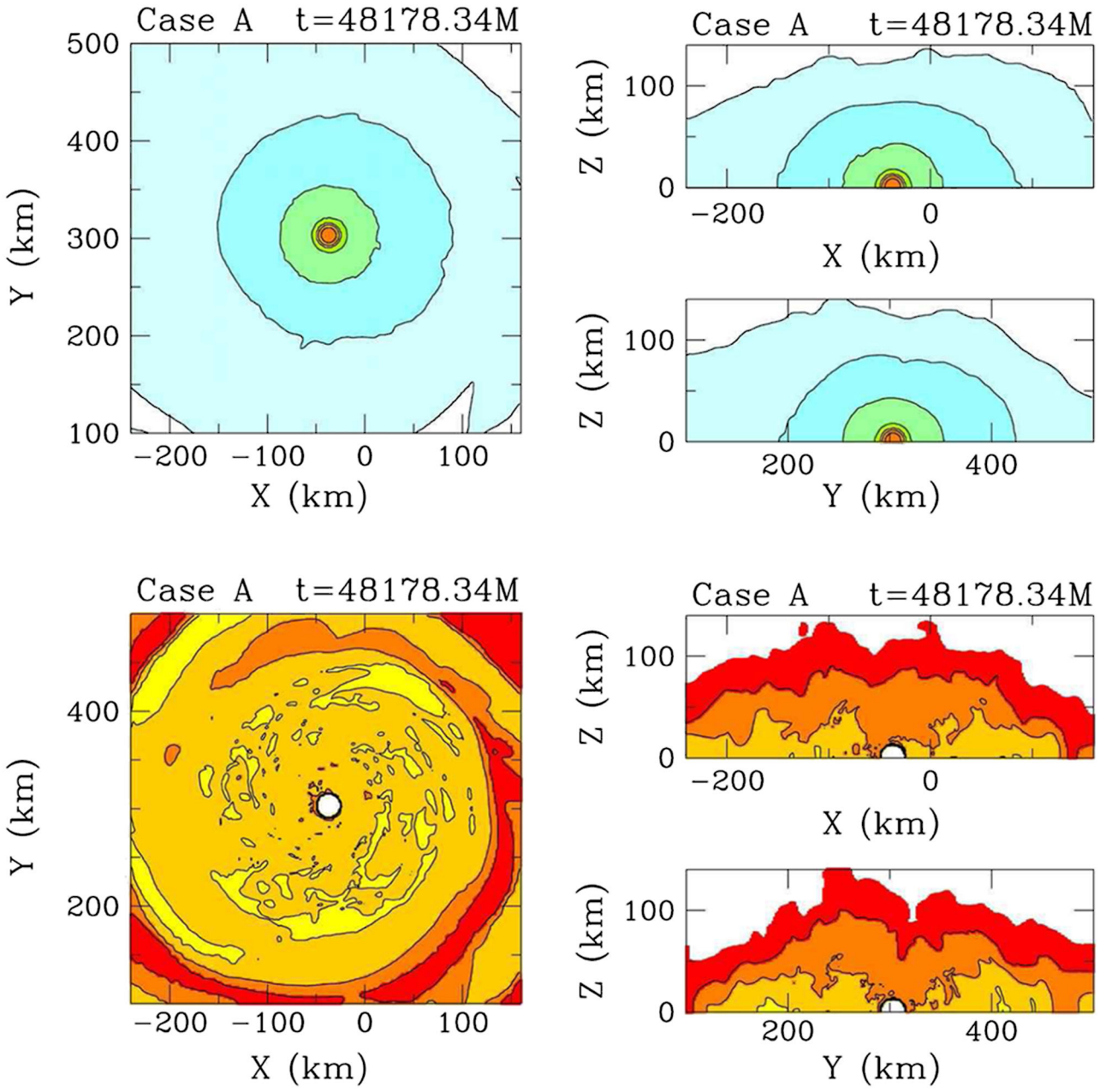

FIG. 5 (color online). First row: Snapshots of rest-mass density profiles at selected times for case A. The contours represent the rest-mass density in the orbital plane and the XZ and YZ meridional planes, plotted according to $\rho_0 = \rho_{0,\max} 10^{-0.69j-0.16} (j = 0, 1, \ldots, 7)$, where $\rho_{0,\max} = 4.645\rho_{\rm nuc}$, and $\rho_{\rm nuc} = 2 \times 10^{14}$ g/cm^3. Second row: Snapshots of $K = P/P_{\rm cold}$ profiles at selected times for case A. The contours represent K in the orbital plane and the XZ and YZ meridional planes, plotted according to $K = 10^{-0.1125j+0.9} (j = 0, 1, \ldots, 7)$. The plots show that the remnant NS core is approximately spherical and cold ($K \approx 1$). Far from the core the remnant is hot. K increases as we move away from the core and the orbital plane. All plots focus in the innermost 200 km from the TZlO center of mass. The color code used is the same as that defined in Fig. 1, with white in the second row indicating $K \approx 1$. Here $M = 2.38 M_\odot = 3.52$ km $= 1.17 \times 10^{-5}$ s.

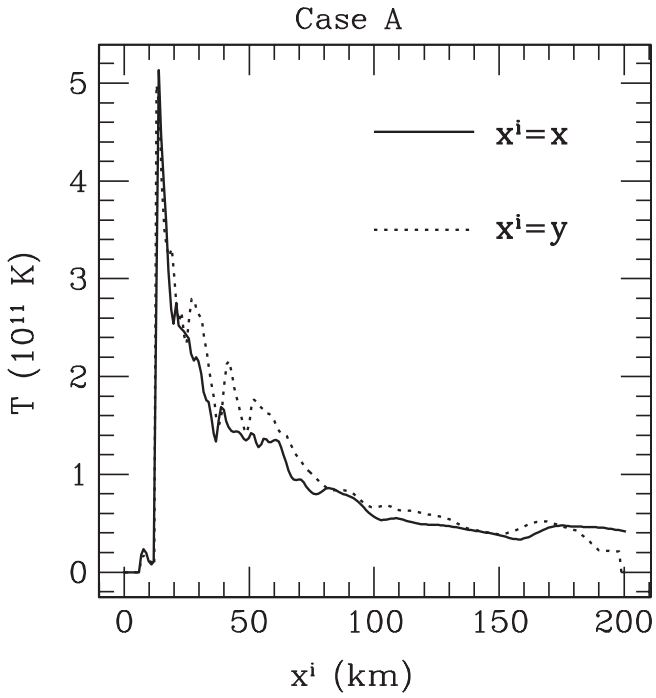

FIG. 6. Temperature (T) profile for case A. The temperature is presented in units of 10^{11} K, where K indicates degrees Kelvin (not to be confused with the EOS entropy parameter K). The solid curve corresponds to the values of T at the end of the simulations and along the x axis for $y = y_c$, $x > x_c$, where x_c (y_c) is the x (y) position of the center of mass of the remnant. The dotted curve corresponds to the values of T along the y axis for $y > y_c$, $x = x_c$. It is clear that typical temperatures are of order 10^{11} K, while the TZlO core is practically at 0 K. For a realistic massive WDNS merger we expect T $\sim 10^9$ K [see discussion following Eq. (71)].

C. Cooling of spinning TZlOs formed in WDNS mergers

To determine whether the spinning TZlO from the WDNS inspiral and merger will collapse to a BH following cooling, we apply our cooling technique setting the cooling time scale to the same value used earlier ($\tau_c = 6000$ km) in Sec. VI. We turn on cooling after about 4.5 orbital time scales and follow the subsequent evolution for about 7 cooling time scales.

Figure 7 plots density contours in the orbital plane at selected times, and Fig. 8 shows the evolution of the maximum rest-mass density and the rest mass contained within spheres with different coordinate radii. These figures demonstrate that both the maximum density and the rest mass within 40 km and 220 km increase as functions of time. As the hot outermost layers become cooler, they contract and accumulate onto the innermost colder parts. For this reason the innermost density contours of like density increase in size (see Fig. 7). The remnant is contracting with time. The contraction is more rapid in the beginning and begins to plateau after about 6 cooling time scales. Therefore, the spinning TZlO does *not* collapse to a BH when thermal support is removed.

Figure 9 shows density and K contours for the innermost regions of the remnant in the XY, XZ, and YZ planes, 6 cooling time scales after cooling was turned on. The shape of the NS core remains spherical throughout the evolution. The XZ and YZ contours demonstrate that the disk and mantle have become thinner, as expected when cooling takes place. Because of this effect, this final configuration is a massive accretion disk onto a NS, rather than a disk around a TZlO.

The bottom row of Fig. 9 shows contours of $K = P/P_{\rm cold}$. Notice that the neutron star core remains cold $K \approx 1$ at the end of the simulation and that elsewhere K has decreased considerably compared to the run without cooling. Here $K_{\rm max} \approx 1.25$, while in the run without cooling $K_{\rm max} \approx 10$. In the innermost region, cold pressure dominates, with $K \approx 1.05$. Given that the rest mass within 220 km of the remnant center of mass is greater than $2.05M_\odot$, which exceeds the maximum supportable mass by our cold EOS, we conclude that the spinning TZlO is *centrifugally supported* from collapse to a BH.

Based on these results and the scalability of our simulations to the realistic scenario, we are led to the tentative prediction that realistic WDNS mergers with total rest mass $\lesssim 2.5M_\odot$, the rest mass in our simulations, will not collapse to a BH following cooling. This conclusion assumes that angular momentum redistribution takes place on a longer time scale than cooling.

Given the absence of outflows in our simulations (with the caveat that we do not model nuclear reactions), the final total rest mass ($\approx 2.5M_\odot$) is larger than the maximum rest mass supportable by our cold EOS, even allowing for maximal uniform rotation. Therefore, we expect that after viscosity and/or magnetic fields redistribute angular momentum, the remnant will collapse to a black hole. This conclusion will be true in the case of realistic WDNS mergers, unless the true nuclear EOS supports a uniformly rotating star with a rest mass exceeding the remnant mass. Many viable EOSs do not support a uniformly rotating cold configuration with rest mass as large as $2.5M_\odot$ [37], the remnant rest mass in our simulations.

VIII. DISCUSSION

To identify the relevant nuclear reaction networks and the dominant cooling mechanisms in realistic inspiraling WDNS binaries, we need to estimate the temperatures of realistic TZlOs. Moreover, to determine the time scale on which angular momentum redistribution occurs we have to consider viscosity and/or magnetic fields. In this section we discuss these issues.

A. Temperature

The characteristic temperature of realistic TZlOs is expected to be of order 10^9 K. This is because the energy

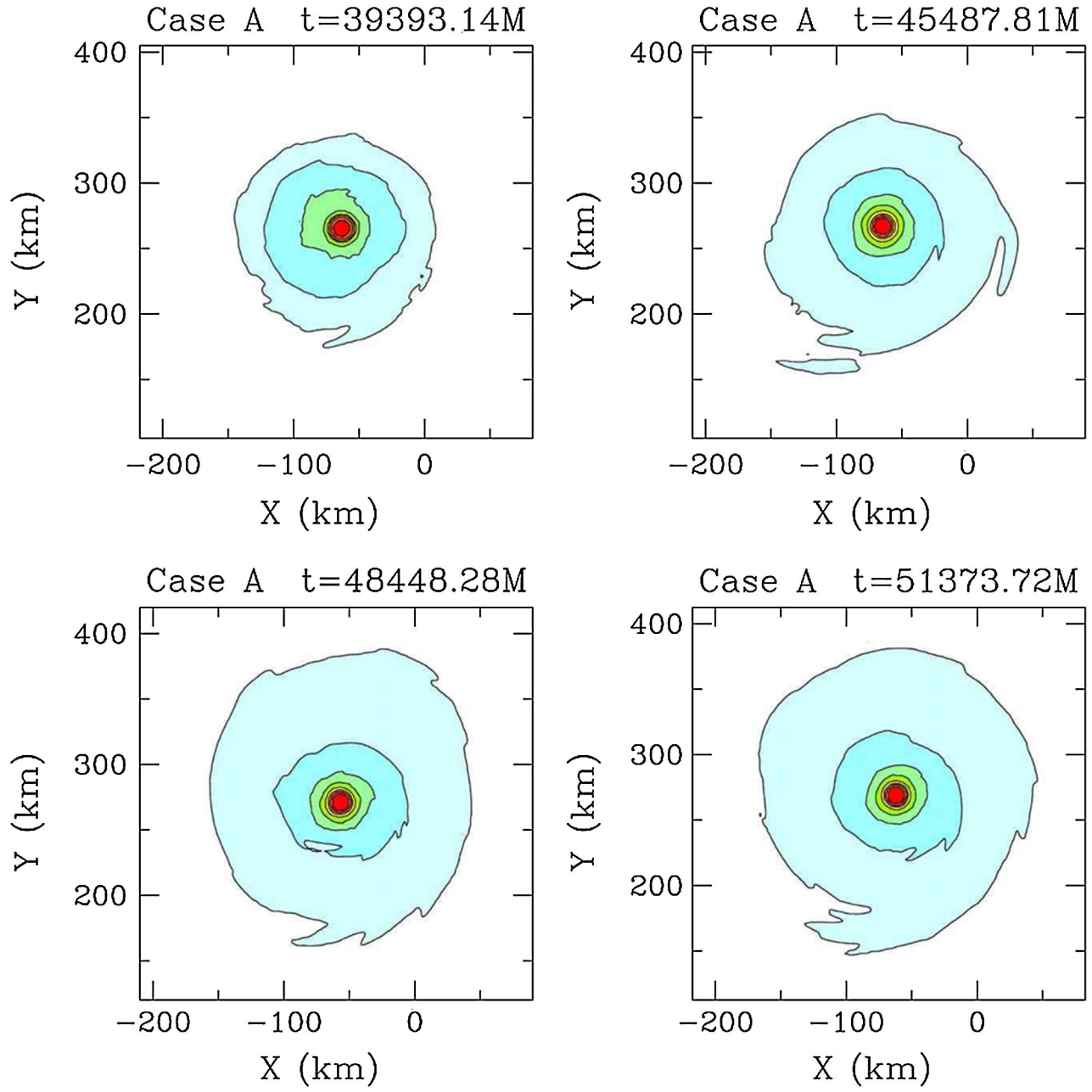

FIG. 7 (color online). Snapshots of rest-mass density profiles at selected times for case A with cooling turned on. The contours represent the rest-mass density in the orbital plane, plotted according to $\rho_0 = \rho_{0,\max} 10^{-0.5j-0.16} (j = 0, 1, \ldots, 8)$, where $\rho_{0,\max} = 4.645\rho_{\rm nuc}$, and $\rho_{\rm nuc} = 2 \times 10^{14}$ g/cm^3. The last two snapshots show that the contraction practically stops after about 6 cooling time scales. The color code used is the same as that defined in Fig. 1 and $M = 2.38 M_\odot = 3.52$ km $= 1.17 \times 10^{-5}$ s.

available for shock heating is of order the gravitational interaction energy when the two stars first touch, $M_{\rm NS} M_{\rm WD}/R_{\rm WD}$. Our simulations demonstrate that the NS is largely unaffected by shock heating and remains cold. Hence, most of the thermal energy is stored in the WD debris. The total thermal energy, $E_{\rm th}$, is then

$$E_{\rm th} \sim \frac{M_{\rm WD}}{m_n} k{\rm T} \sim \frac{M_{\rm NS} M_{\rm WD}}{R_{\rm WD}}. \tag{70}$$

From this last equation we can estimate the characteristic temperature as

$${\rm T} \sim \frac{C_{\rm WD} m_n}{qk}, \tag{71}$$

where $C_{\rm WD} = M_{\rm WD}/R_{\rm WD}$ is the WD compaction. All things being equal (i.e., no mass loss, same mass ratio, etc.), characteristic TZlO temperatures should be proportional to the WD compaction. The compaction of a realistic

$1.0M_\odot$ WD that obeys the Chandrasekhar EOS is $C_{\rm WD} \simeq 10^{-4}$ [34,68]. If the NS mass is $1.4M_\odot$ then $q \simeq 0.7$, and Eq. (71) predicts $T \simeq 1.55 \times 10^9$ K.

Note that applying Eq. (71) to case A, where $C_{\rm pWD} \simeq 10^{-2}$, yields a temperature $T \simeq 1.55 \times 10^{11}$ K, i.e., in good agreement with our simulations [89].

B. Nuclear fusion

Are realistic WDNS binary remnant densities and temperatures high enough for nuclear reactions to take place? The shock-heated matter is composed of hot (diluted) WD debris, so its density is of order typical WD densities, i.e., 10^6 g/cm^3. A $1.0M_\odot$ WD is sufficiently massive that its main constituent elements are carbon and oxygen. While the temperatures and densities we expect for realistic mergers are probably not high enough for oxygen burning to become important, they are sufficiently high for carbon fusion to become dynamically relevant.

Nonexplosive nuclear reactions in the context of WDNS mergers were recently considered in [90]. A one-dimensional (1D) steady-state model of accretion onto a NS was introduced, allowing for disk wind outflows that do not exert any torque on the disk. It was found that heating from nuclear burning is so important that a disk wind eventually unbinds 50%–80% of the original WD mass. It was suggested that these ejecta may include small quantities of radioactive ^{56}Ni. In such scenarios, detectable EM signals will likely follow a WDNS merger. Although this 1D steady-state model includes much of the important physics (albeit in parametrized form), it is simplified and does not apply to the large mass-ratio mergers simulated here. However, as in the 1D model we do expect that nuclear burning will also be nonexplosive in a realistic WDNS merger, as we now explain.

In a *head-on* collision of a WDNS binary with companions of comparable mass that collide at free-fall velocity, the kinetic energy of motion is converted by shocks into thermal energy in the WD remnant. This shock heating at merger guarantees that a degenerate WD initially in hydrostatic equilibrium will acquire shock-induced thermal pressure comparable in magnitude to its original equilibrium degeneracy pressure, thereby lifting the degeneracy, i.e.,

$$\frac{P_{\rm th}}{\rho_0} \sim \frac{k\mathrm{T}}{m_n} \sim v_{\rm ff}^2 \sim \frac{GM}{R_{\rm WD}} \sim \frac{P_{\rm eq,WD}}{\rho_0} \sim \frac{P_{\rm cold}}{\rho_0}. \tag{72}$$

The net effect should be to reduce the likelihood of explosive carbon burning, since a carbon flash requires a degenerate environment. The reason for this is that if gas pressure becomes a significant component of the total pressure, then the pressure will be sensitive to the temperature. Therefore, if carbon fusion takes place, the released heat will increase the gas temperature which will, in turn, increase the pressure. As a result the gas will expand, decreasing its density and temperature, and eventually

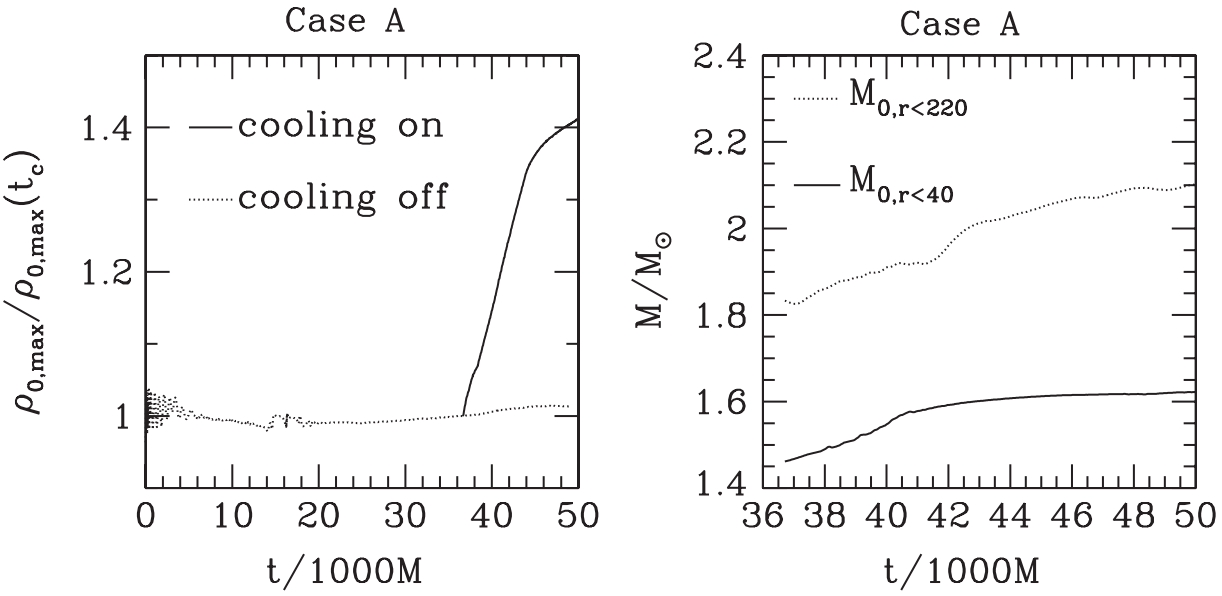

FIG. 8. Left: Evolution of maximum value of rest-mass density with cooling (solid curve) and without cooling (dotted curve) for case A. Here $\rho_{0,\rm max}$ is the maximum value of the rest-mass density, and $\rho_{0,\rm max}(t_c) = 5.88 \times 10^{-4}$ km^{-2} $= 7.92 \times 10^{14}$ g/cm^3 is the maximum value of rest-mass density at the time ($t_c = 36\,705M$) when cooling is turned on. Right: Evolution of rest mass within different radii with cooling turned on. Here $M_{0,r<r_0}$ stands for the rest mass contained within a coordinate sphere of radius r_0 in units of km, centered on the remnant's center of mass. These plots demonstrate that the TZlO remnant contracts when cooling is turned on. However, the values of $\rho_{0,\rm max}$ and $M_{0,r<r_0}$ begin to plateau after 6 cooling time scales, indicating no further contraction proceeds after this time. Here $M = 2.38M_\odot = 3.52$ km $= 1.17 \times 10^{-5}$ s is the sum of the ADM masses of the isolated stars.

carbon fusion will be turned off. Such a process is self-regulated, a well-known fact.

Shock heating plays a similar role in the merger of an inspiraling binary, only it is not as strong and the fraction of the thermal pressure generated will be smaller, due to the role of angular momentum in lessening the impact and contributing to the support of the remnant. Using our estimated temperature $T \approx 10^9$ K and characteristic density 10^6 g/cm^3 for realistic TZIOs, the ratio of thermal gas pressure to the electron degenerate pressure is 4. This

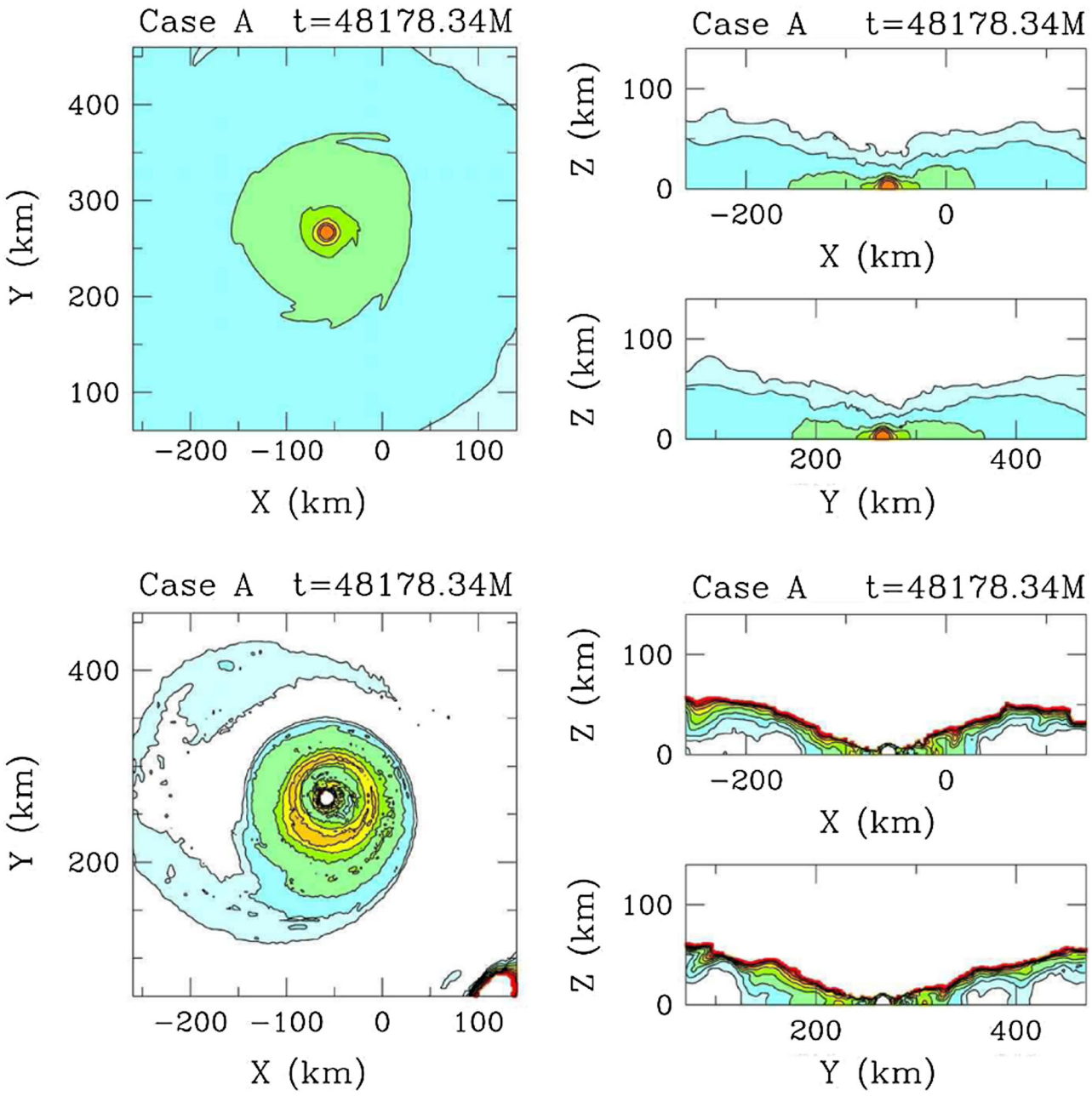

FIG. 9 (color online). First row: Snapshots of rest-mass density profiles at selected times for case A with cooling. The contours represent the rest-mass density in the orbital plane and the XZ and YZ meridional planes, plotted according to $\rho_0 = \rho_{0,\max} 10^{-0.69j-0.16} (j = 0, 1, \ldots, 7)$, where $\rho_{0,\max} = 4.645\rho_{\rm nuc}$, and $\rho_{\rm nuc} = 2 \times 10^{14}$ g/cm^3. Second row: Snapshots of $K = P/P_{\rm cold}$ profiles at selected times for case A with cooling. The contours represent K in the orbital plane and the XZ and YZ meridional planes, plotted according to $K = 10^{-0.014j+0.1} (j = 0, 1, \ldots, 7)$. The plots show that the remnant NS core is approximately spherical and cold ($K \approx 1$). Far from the core the remnant is hotter. K increases as we move away from the core and the orbital plane. In contrast to the case without cooling (see Fig. 5), the maximum value for K here is $K_{\max} \approx 1.25$. For easy comparison with the case without cooling (Fig. 5), all plots focus in the innermost 200 km from the remnant center of mass. The color code used is the same as that defined in Fig. 1, with white in the second row indicating $K \approx 1$. Here $M = 2.38 M_\odot = 3.52$ km $= 1.17 \times 10^{-5}$ s.

implies that the WD debris would be nondegenerate. Under these conditions a carbon flash is likely suppressed, but further simulations would be useful to confirm this.

C. Neutrino cooling

For the estimated characteristic temperature $T = 10^9$ K and density $\rho_0 = 10^6$ g/cm^3, the dominant cooling mechanism likely will involve neutrino emission. At these densities and temperatures, thermal neutrino processes (pair neutrinos, photoneutrinos, plasmon decay, and bremsstrahlung [68]) are important, with pair annihilation ($e^- + e^+ \rightarrow \nu + \bar{\nu}$) being slightly more important than the other processes (see Fig. 1 in [91] and Fig. 3a in [92]). The pair neutrino cooling rate can be estimated as [93]

$$\epsilon_\nu^{\rm pair} \approx 4.45 \times 10^9 \frac{T_9{}^9}{\rho_6} [{\rm erg/g/s}], \tag{73}$$

where $T_9 = T/10^9$ K, $\rho_6 = \rho_0/10^6$ g cm^{-3}, and the high-temperature and nondegenerate limit has been assumed.

The specific thermal energy is approximately given by $\epsilon_{\rm th} = 3kT/m_n$. Based on this, the cooling time scale can be estimated as

$$\tau_{\rm cooling} = \frac{\epsilon_{\rm th}}{\epsilon_\nu^{\rm pair}} \approx 1.76 \text{ yr} \frac{\rho_6}{T_9{}^8}. \tag{74}$$

Notice that for $T_9 = 0.1$, $\tau_{\rm cooling} \approx 10^8$ yr. Thus the object cools fast when it is very hot, but when the temperature drops to 10^8 K it takes hundreds of millions of years for cooling to take place.

Based on these considerations and Eq. (73), the net conclusion is that the neutrino cooling time scale is highly temperature sensitive, and our pWDNS inspiral simulation may only provide a crude estimate of temperature. Therefore, simulations with more physics are necessary to precisely calculate realistic TZlO temperatures, so that the relevant cooling time scales may be better estimated.

Adopting the cooling rate (73) we can estimate whether neutrinos from WDNS mergers are detectable. The number of detectable neutrinos (N_d) are approximately given by

$$N_d \approx \frac{L_\nu \sigma_\nu \Delta T}{4\pi D^2 \bar{\epsilon}_\nu}, \tag{75}$$

where L_ν is the total neutrino luminosity, σ_ν the neutrino detection cross section, ΔT the time interval over which neutrinos are emitted, D the distance to the binary, and $\bar{\epsilon}_\nu$ the average neutrino energy. Given that $\sigma_\nu \approx 10^{-44}$ cm^2, and the expected neutrino energy from pair annihilation is $\epsilon_\nu \approx 0.5$ MeV, we estimate

$$N_d \approx 10^{-32} \frac{T_9{}^9}{\rho_6} \left(\frac{M}{M_\odot}\right) \left(\frac{\sigma_\nu}{10^{-44}\ {\rm cm}^2}\right) \left(\frac{\Delta T}{1\ {\rm yr}}\right) \left(\frac{\bar{\epsilon}_\nu}{0.5\ {\rm MeV}}\right)^{-1} \times \left(\frac{D}{1\ {\rm kpc}}\right)^{-2}, \tag{76}$$

where we have assumed that the entire TZlO mantle emits neutrinos at the same rate for a year.

Given this result, we conclude that neutrinos emitted in WDNS mergers are unlikely to be detectable. However, simulations with detailed microphysics [94] would be useful to confirm this.

D. Angular momentum redistribution

Our inspiraling WDNS merger simulation with cooling turned on shows that the remnant does not collapse to a BH following cooling, because it is centrifugally supported. Given that the mass of the remnant is larger than the maximum mass supportable by our cold EOS, it is likely that delayed collapse will take place after angular momentum is redistributed.

Angular momentum redistribution will occur on the viscous or Alfvén time scale. Assuming an α disk, the viscous time scale (neglecting the disk self-gravity) is given by

$$t_{\rm vis} \simeq \alpha^{-1} \left(\frac{H}{R}\right)^{-2} \sqrt{\frac{R^3}{M_{\rm TZlO}}}, \tag{77}$$

where H is the disk scale height, R the characteristic disk radius, and α the turbulent viscosity parameter. Using the values for H/R and $M_{\rm TZlO}$ found in our simulations we estimate that in realistic WDNS mergers the viscous time scale is

$$t_{\rm vis} \simeq 20s \left(\frac{\alpha}{0.1}\right)^{-1} \left(\frac{H/R}{1.0}\right)^{-2} \left(\frac{R}{10^4\ {\rm km}}\right)^{3/2} \left(\frac{M_{\rm TZlO}}{1.8 M_\odot}\right)^{1/2}, \tag{78}$$

where $R \approx 2R_{\rm WD}$, i.e., near the Roche limit for a $1.0M_\odot$ WD with a $1.4M_\odot$ NS.

The Alfvén time scale ($t_A = R/v_A$, where v_A is the Alfvén speed) is given by

$$t_A \simeq \beta^{-1/2} \left(\frac{H}{R}\right)^{-1} \sqrt{\frac{R^3}{M_{\rm TZlO}}}, \tag{79}$$

where the β parameter

$$\beta \equiv \frac{B^2}{8\pi P} \tag{80}$$

was introduced to obtain the last expression. If we use the same values for R, H/R, and $M_{\rm TZlO}$ as in Eq. (78), the Alfvén time scale becomes

$$t_A \simeq 6.5s\left(\frac{\beta}{0.1}\right)^{-1/2}\left(\frac{H/R}{1.0}\right)^{-1}\left(\frac{R}{10^4\ \mathrm{km}}\right)^{3/2}\left(\frac{M_{\mathrm{TZlO}}}{1.8M_\odot}\right)^{-1/2}. \quad (81)$$

We emphasize that the dimensionless parameters α and β above are unknown and may both be $\ll 1$, in which case the angular momentum redistribution time scale may be as long as the cooling time scale. For example, observations of magnetic WDs indicate that surface magnetic field strengths are $B \sim 10^4$–10^9 G [95] or $\beta \sim 10^{-17}$–$10^{-7} \ll 1$, where we calculated the thermal pressure as $P = \rho_0 k\mathrm{T}/m_n$ with $\rho_0 = 10^6$ g/cm^3, $\mathrm{T} = 10^9$ K. If $\beta \lesssim 10^{-15}$, then the Alfvén time scale is longer than 1 yr, i.e., the cooling time scale for $\mathrm{T}_9 = 1$. However, field amplification via winding and instabilities (e.g., magnetorotational instability) is always possible. Hence, we must await detailed calculations for reliable estimates of the angular momentum redistribution time scale.

IX. SUMMARY AND CONCLUSIONS

This work is a follow-up to our study of binary WDNS head-on collisions [33], focusing on the dynamics of an initially circular, quasiequilibrium WDNS binary through inspiral and merger. In particular, we begin with a circular binary in which the WD has just filled its Roche lobe (the Roche limit) and with systems whose total mass exceeds the maximum mass that a cold EOS can support. The goal is to determine whether a WDNS merger leads to either prompt collapse to a BH or a spinning quasiequilibrium configuration consisting of a cold NS surrounded by a hot gaseous mantle of WD debris, or something else.

Because of the vast range of dynamical time and length scales, hydrodynamic simulations in full GR of realistic WDNS mergers (head-on or otherwise) are computationally prohibitive. For this reason, we tackle the problem using the same approach as in our investigation of binary WDNS head-on collisions. In particular, we adopt the pWD approximation with the 10:1 EOS constructed in [33]. This EOS captures the main physical features of NSs, but scales down the size of WDs so that the ratio of the isotropic radius of a TOV $0.98M_\odot$ pWD to that of a TOV $1.5M_\odot$ NS is 10:1 (hence the name of the EOS), rather than the more realistic ratio 500:1. These pWDs enable us to reduce the range of length and time scales involved while maintaining all length- and time-scale inequalities, rendering the computations tractable and the results scalable.

If the pWDNS merger does not result in prompt collapse to a black hole, it is unlikely that the corresponding WDNS merger will collapse promptly.

The reason for this expectation is that the pWD approximation is based on scaling. In particular, both the collision velocity and the preshocked WD sound speed scale as $\sim(M/R_{\mathrm{WD}})^{1/2}$. This implies that the Mach number is invariant under scaling of R_{WD} and so is the degree of shock heating. So the thermal energy as well as the rotational kinetic energy (T) and the gravitational potential energy (W) all scale as $\sim M^2/R_{\mathrm{WD}}$, when the binary merges. Thus $T/|W|$ is also invariant under scaling of R_{WD}. These considerations simply mean that with respect to gravity the relative importance of thermal and rotational support in a WDNS merger remnant is approximately invariant, when the masses of the binary components are fixed and the only quantity that changes is the WD radius. As a consequence, the results obtained when adopting pWDNS systems can be scaled up to realistic WDNS systems.

To predict whether a TZlO, which does not collapse to a BH promptly, will collapse following cooling, we introduced an artificial cooling mechanism (see Sec. V). If following cooling the remnant collapses, we expect that delayed collapse in the corresponding WDNS case likely will take place on a cooling time scale.

To test our cooling prescription, we applied it to the TZlOs formed in the WDNS head-on collision simulations we performed in [33]. We demonstrated that these remnants collapse to a black hole when the excess thermal energy is radiated away, as expected.

Finally, we simulated the merger of an initially quasiequilibrium, corotational pWDNS system in circular orbit at the Roche limit, composed of a $1.4M_\odot$ NS and a $0.98M_\odot$ pWD. We find that the remnant of the pWDNS inspiral is a spinning TZlO which is surrounded by an extended, hot disk. The coordinate radius of the TZlO remnant and disk is approximately 300 km and 1000 km, respectively. We estimated the disk mass to be $\gtrsim 50\%$ of the initial original WD rest mass. In contrast to our binary WDNS head-on collision investigations, no outflows were observed in the circular case. The final total ADM mass ($\sim 2.4M_\odot$) is greater than the maximum mass supportable by a cold, degenerate star with our adopted NS EOS. However, the remnant does not collapse promptly to a black hole. This is because the remnant is both thermally and centrifugally supported. To determine whether centrifugal support by itself supports the remnant from collapse, we enabled our radiative cooling mechanism and found that the object does not collapse to a black hole following cooling. Therefore, the extra support provided by rotation is sufficient for holding the collapse.

Although the TZlO does not collapse following cooling, ultimate collapse to a BH is almost certain, since the final total mass is larger than the maximum possible mass supportable by our cold EOS (and many nuclear EOSs), even allowing for maximal uniform rotation. Therefore, delayed collapse likely will take place after viscosity or magnetic fields redistribute the angular momentum and/or following cooling. This conclusion will be true in the case of realistic WDNS mergers, unless the true nuclear EOS supports a uniformly rotating star with a rest mass exceeding the remnant mass. Many viable EOSs do not support rest masses as large as $2.5M_\odot$ [37], the remnant rest mass in our simulations.

Our results hold true provided that nuclear burning remains unimportant in the postmerger event. We estimated that typical realistic TZlO temperatures will be of order 10^9 K. For typical WD densities of order 10^6 g/cm^3, carbon is ignited and can become an important source of heating. Though nuclear burning likely will play some role in the postmerger evolution of a massive WDNS system, we do not expect a carbon flash to occur. The reason for this is that shocks at merger lift the degeneracy of the WD matter. Given that a carbon flash requires a cold, degenerate environment, the net effect should be to reduce the likelihood of explosive carbon burning. Nevertheless, further simulations would be useful.

The neutrino cooling time scale is highly temperature sensitive, and our pWDNS inspiral simulation may only provide a crude estimate of temperature. Therefore, simulations with more physics are necessary to precisely calculate realistic TZlO temperatures, so that the relevant cooling time scales may be better determined. Finally, while our simulations indicate that prompt collapse to a black hole is not possible for WDNS systems with total rest mass $\lesssim 2.5M_\odot$, it is likely that systems with greater mass can collapse promptly. Therefore, more simulations in full GR are necessary before a definitive solution to the problem can be given. We plan to address these issues in a future work.

ACKNOWLEDGMENTS

We would like to thank Brian D. Farris and Thomas W. Baumgarte for helpful discussions. We are also grateful to Morgan MacLeod for providing the Newtonian binary pWDNS equilibrium configurations, which we used to generate our CTS initial data. This paper was supported in part by NSF Grants No. PHY06-50377 and No. PHY09-63136 as well as NASA Grants No.NNX07AG96G and No. NNX10AI73G to the University of Illinois at Urbana-Champaign.

[1] B. Abbott *et al.* (LIGO Scientific Collaboration), Phys. Rev. D **77**, 062002 (2008).
[2] D. A. Brown *et al.*, Classical Quantum Gravity **21**, S1625 (2004).
[3] F. Acernese *et al.* (VIRGO Collaboration), Classical Quantum Gravity **23**, S635 (2006).
[4] F. Beauville (LIGO-VIRGO Working Group) Classical Quantum Gravity **25**, 045001 (2008).
[5] H. Lück *et al.* (GEO600 Collaboration), Classical Quantum Gravity **23**, S71 (2006).
[6] M. Ando (TAMA Collaboration), Classical Quantum Gravity **19**, 1409 (2002).
[7] D. Tatsumi *et al.* (TAMA Collaboration), Classical Quantum Gravity **24**, S399 (2007).
[8] http://www.gravity.uwa.edu.au/docs/aigo_prospectus.pdf.
[9] G. Heinzel, C. Braxmaier, K. Danzmann, P. Gath, J. Hough, O. Jennrich, U. Johann, A. Rüdiger, M. Salusti, and H. Schulte, Classical Quantum Gravity **23**, S119 (2006).
[10] S. Kawamura *et al.* (DECIGO Collaboration), Classical Quantum Gravity **23**, S125 (2006).
[11] T. W. L. Baumgarte and S. L. Shapiro, *Numerical Relativity* (Cambridge University Press, Cambridge, England, 2010).
[12] I. Hinder, Classical Quantum Gravity **27**, 114 004 (2010).
[13] M. D. Duez, Classical Quantum Gravity **27**, 114 002 (2010).
[14] E. Rantsiou, S. Kobayashi, P. Laguna, and F. A. Rasio, Astrophys. J. **680**, 1326 (2008).
[15] F. Löffler, L. Rezzolla, and M. Ansorg, Phys. Rev. D **74**, 104018 (2006).
[16] J. A. Faber, T. W. Baumgarte, S. L. Shapiro, K. Taniguchi, and F. A. Rasio, Phys. Rev. D **73**, 024012 (2006).
[17] J. A. Faber, T. W. Baumgarte, S. L. Shapiro, and K. Taniguchi, Astrophys. J. Lett. **641**, L93 (2006).
[18] M. Shibata and K. Uryu, Phys. Rev. D **74**, 121503(R) (2006).
[19] M. Shibata and K. Uryu, Classical Quantum Gravity **24**, S125 (2007).
[20] M. Shibata and K. Taniguchi, Phys. Rev. D **77**, 084015 (2008).
[21] T. Yamamoto, M. Shibata, and K. Taniguchi, Phys. Rev. D **78**, 064054 (2008).
[22] Z. B. Etienne, J. A. Faber, Y. T. Liu, S. L. Shapiro, K. Taniguchi, and T. W. Baumgarte, Phys. Rev. D **77**, 084002 (2008).
[23] Z. B. Etienne, Y. T. Liu, S. L. Shapiro, and T. W. Baumgarte, Phys. Rev. D **79**, 044024 (2009).
[24] M. D. Duez, F. Foucart, L. E. Kidder, H. P. Pfeiffer, M. A. Scheel, and S. A. Teukolsky, Phys. Rev. D **78**, 104015 (2008).
[25] M. Shibata, K. Kyutoku, T. Yamamoto, and K. Taniguchi, Phys. Rev. D **79**, 044030 (2009).
[26] K. Kyutoku, M. Shibata, and K. Taniguchi, Phys. Rev. D **79**, 124018 (2009).
[27] P. M. Motl, M. Anderson, M. Besselman, S. Chawla, E. W. Hirschmann, L. Lehner, S. L. Liebling, D. Neilsen, and J. E. Tohline, Bull. Am. Astron. Soc. **41**, 295 (2010).
[28] S. Chawla, M. Anderson, M. Besselman, L. Lehner, S. L. Liebling, P. M. Motl, and D. Neilsen, Phys. Rev. Lett. **105**, 111101 (2010).
[29] M. D. Duez, F. Foucart, L. E. Kidder, C. D. Ott, and S. A. Teukolsky, Classical Quantum Gravity **27**, 114 106 (2010).
[30] F. Pannarale, A. Tonita, and L. Rezzolla, Astrophys. J. **727**, 95 (2011).

[31] F. Foucart, M. D. Duez, L. E. Kidder, and S. A. Teukolsky, Phys. Rev. D **83**, 024005 (2011).

[32] K. Kyutoku, M. Shibata, and K. Taniguchi, Phys. Rev. D **82**, 044049 (2010).

[33] V. Paschalidis, Z. Etienne, Y. T. Liu, and S. L. Shapiro, Phys. Rev. D **83**, 064002 (2011).

[34] V. Paschalidis, M. MacLeod, T. W. Baumgarte, and S. L. Shapiro, Phys. Rev. D **80**, 024006 (2009).

[35] P. B. Demorest, T. Pennucci, S. M. Ransom, M. S. E. Roberts, and J. W. T. Hessels, Nature (London) **467**, 1081 (2010).

[36] T. W. Baumgarte, S. L. Shapiro, and M. Shibata, Astrophys. J. Lett. **528**, L29 (2000).

[37] I. A. Morrison, T. W. Baumgarte, and S. L. Shapiro, Astrophys. J. **610**, 941 (2004).

[38] G. B. Cook, S. L. Shapiro, and S. A. Teukolsky, Astrophys. J. **422**, 227 (1994).

[39] A. Akmal, V. R. Pandharipande, and D. G. Ravenhall, Phys. Rev. C **58**, 1804 (1998).

[40] C. P. Lorenz, D. G. Ravenhall, and C. J. Pethick, Phys. Rev. Lett. **70**, 379 (1993).

[41] R. B. Wiringa, V. Fiks, and A. Fabrocini, Phys. Rev. C **38**, 1010 (1988).

[42] V. R. Pandharipande and R. A. Smith, Bull. Am. Astron. Soc. **7**, 240 (1975).

[43] H. A. Bethe and M. B. Johnson, Nucl. Phys. **A230**, 1 (1974).

[44] V. R. Pandharipande, Nucl. Phys. **A174**, 641 (1971).

[45] G. Nelemans, L. R. Yungelson, and S. F. P. Zwart, Astron. Astrophys. **375**, 890 (2001).

[46] A. Cooray, Mon. Not. R. Astron. Soc. **354**, 25 (2004).

[47] T. A. Thompson, M. D. Kistler, and K. Z. Stanek, arXiv:0912.0009.

[48] K. Thorne and A. Zytkow, Astrophys. J. **212**, 832 (1977).

[49] S. Rappaport, P. C. Joss, and R. F.Webbink, Astrophys. J. **254**, 616 (1982).

[50] S. Rappaport, F. Verbunt, and P. C. Joss, Astrophys. J. **275**, 713 (1983).

[51] F. Verbunt and S. Rappaport, Astrophys. J. **332**, 193 (1988).

[52] P. Podsiadlowski, P. C. Joss, and J. J. L. Hsu, Astrophys. J. **391**, 246 (1992).

[53] T. R.Marsh, G. Nelemans, and D. Steeghs, Mon. Not. R. Astron. Soc. **350**, 113 (2004).

[54] W. Benz, R. Bowers, A. Cameron, and W. Press, Astrophys. J. **348**, 647 (1990).

[55] F. A. Rasio and S. L. Shapiro, Astrophys. J. **438**, 887 (1995).

[56] L. Segretain, G. Chabrier, and R. Mochkovitch, Astrophys. J. **481**, 355 (1997).

[57] J. Guerrero, E. Garcia-Berro, and J. Isern, Astron. Astrophys. **413**, 257 (2004).

[58] S.-C. Yoon, P. Podsiadlowski, and S. Rosswog, Mon. Not. R. Astron. Soc. **380**, 933 (2007).

[59] M. Dan, S. Rosswog, and M. Brüggen, J. Phys. Conf. Ser. **172**, 012 034 (2009).

[60] Z. B. Etienne, Y. T. Liu, and S. L. Shapiro, Phys. Rev. D **82**, 084031 (2010).

[61] The $1.97M_{\odot}$ NS [35] was discovered after we started our pWDNS calculations. This is why the maximum mass of our EOS is smaller than $1.97M_{\odot}$.

[62] L. Caito, M. G. Bernardini, C. L. Bianco, M. G. Dainotti, R. Guida, and R. Ruffini, Astron. Astrophys. **498**, 501 (2009).

[63] G. de Barros, L. Amati, M. G Bernardini, C. L. Bianco, L. Caito, L. Izzo, B. Patricelli, and R. Ruffini, Astron. Astrophys. **529**, A130 (2011)

[64] Even though the range of time and length scales is reduced when using pWDs, the resolution requirements to accurately follow the system and preserve angular momentum rendered our calculations very expensive. In particular, it required 9 months of wall clock time for our simulations to finish.

[65] M. Shibata, T. W. Baumgarte, and S. L. Shapiro, Phys. Rev. D **61**, 044012 (2000).

[66] M. D. Duez, Y. T. Liu, S. L. Shapiro, M. Shibata, and B. C. Stephens, Phys. Rev. Lett. **96**, 031101 (2006).

[67] M. D. Duez, Y. T. Liu, S. L. Shapiro, and B. C. Stephens, Phys. Rev. D **69**, 104030 (2004).

[68] S. L. Shapiro and S. A. Teukolsky, *Black Holes, White Dwarfs, and Neutron Stars* (John Wiley and Sons, New York, 1983).

[69] J. S. Read, B. D. Lackey, B. J. Owen, and J. L. Friedman, Phys. Rev. D **79**, 124032 (2009).

[70] R. Arnowitt, S. Deser, and C. Misner, *Gravitation: An Introduction to Current Research* (Wiley, New York, 1962).

[71] J. M. Bowen and J. W. York, Phys. Rev. D **21**, 2047 (1980).

[72] T. W. Baumgarte, G. B. Cook, M. A. Scheel, S. L. Shapiro, and S. A. Teukolsky, Phys. Rev. D **57**, 7299 (1998).

[73] S. Balay, K. Buschelman, W. D. Gropp, D. Kaushik, M. G. Knepley, L. C. McInnes, B. F. Smith, and H. Zhang, http://www.mcs.anl.gov/petsc.

[74] S. Balay, K. Buschelman, V. Eijkhout, W. D. Gropp, D. Kaushik, M. G. Knepley, L. C. McInnes, B. F. Smith, and H. Zhang, PETSc Users Manual, Tech. Rep. ANL-95/11—Revision 3.0.0 (Argonne National Laboratory, 2008).

[75] S. Balay, W. D. Gropp, L. C. McInnes, and B. F. Smith, in *Modern Software Tools in Scientific Computing*, edited by E. Arge, A. M. Bruaset, and H. P. Langtangen (Birkhäuser Press, 1997) p. 163.

[76] M. D. Duez, Y. T. Liu, S. L. Shapiro, and B. C. Stephens, Phys. Rev. D **72**, 024028 (2005).

[77] M. Shibata and T. Nakamura, Phys. Rev. D **52**, 5428 (1995).

[78] T. W. Baumgarte and S. L. Shapiro, Phys. Rev. D **59**, 024007 (1998).

[79] J. R. van Meter, J. G. Baker, M. Koppitz, and D.-I. Choi, Phys. Rev. D **73**, 124011 (2006).

[80] http://www.cactuscode.org/.

[81] E. Schnetter, S. H. Hawley, and I. Hawke, Classical Quantum Gravity **21**, 1465 (2004).

[82] P. Colella and P. R. Woodward, J. Comput. Phys. **54**, 174 (1984).

[83] A. Harten, P. D. Lax, and B. van Leer, SIAM Rev. **25**, 35 (1983).

[84] J. A. Font, M. Miller, W.-M. Suen, and M. Tobias, Phys. Rev. D **61**, 044011 (2000).

[85] B. C. Stephens, S. L. Shapiro, and Y. T. Liu, Phys. Rev. D **77**, 044001 (2008).

[86] D. Mihalas and B. W. Mihalas, *Foundations of Radiation Hydrodynamics* (Dover, New York, 1999).
[87] S. L. Shapiro, Astrophys. J. **472**, 308 (1996).
[88] B. D. Farris, T. K. Li, Y. T. Liu, and S. L. Shapiro, Phys. Rev. D **78**, 024023 (2008).
[89] In [33] we estimated the thermal energy of the TZlO as $E_{\rm th} \sim \frac{(M_{\rm NS}+M_{\rm WD})}{m_n} kT$. This estimate does not account for the fact that most of the thermal energy is stored in the WD debris, so the predicted temperature is slightly smaller than that found in our simulations. Our current estimate [Eq. (71)] yields results in good agreement not only with our present simulations, but also with our simulations in [33].
[90] B. D. Metzger, arXiv:1105.6096.
[91] Z. Barkat, Annu. Rev. Astron. Astrophys. **13**, 45 (1975).
[92] G. Beaudet, V. Petrosian, and E. E. Salpeter, Astrophys. J. **150**, 979 (1967).
[93] R. Kippenhahn and A. Weigert, *Stellar Structure and Evolution* (Springer-Verlag, Berlin, 1991).
[94] N. Itoh, H. Hayashi, A. Nishikawa, and Y. Kohyama, Astrophys. J. Suppl. Ser. **102**, 411 (1996).
[95] D. T. Wickramasinghe and L. Ferrario, Publ. Astron. Soc. Pac. **112**, 873 (2000).